Abstract

Using Cryo-Electron Microscopy to Study Microtubule Heterogeneity

Garrett Evan Debs

2020

Microtubules are dynamic, filamentous polymers that are involved in numerous essential cellular activities. Over the past few years, high-resolution structures of microtubules have been solved with various microtubule associated proteins (MAPs), microtubule stabilizing agents, and nucleotide states using cryo-electron microscopy (cryo-EM). However, the results of these structures indicate that microtubules are not idealized, helical tubes, and distortions in the lattice appear common. Here I present a cryo-EM 3D reconstruction method ('protofilament refinement') that segments the microtubule wall, allowing us to quantify and correct for distortions and other sources of heterogeneity at the single-subunit level. This method has allowed us to increase the resolution of microtubule cryo-EM reconstructions to better than 2.9 Å with Taxol-stabilized microtubules, despite the substantial helical disorder present in this biochemical state. Additionally, quantification of microtubule lattice distortions by this method indicates that nearly all microtubules deviate from a perfect cylinder, with measured microtubule wall deformations frequently exceeding the largest values previously measured. Finally, this distortion analysis reveals that at least two major conformational states of tubulin co-exist under the standard biochemical conditions frequently used in the literature.

In addition to protofilament refinement, I also worked to develop a 'layer line masking' method, that provides an alternative means of subtracting microtubule images. Microtubule subtraction can be important when trying to reconstruct large microtubule binding proteins, that irregularly bind to the surface of microtubules. During this work, the layer line masking method was capable of reconstructing irregularly bound spastin particles from synthetic microtubule images to high resolution. While this technique will need to be further verified using experimental data, these promising results show the potential utility of this method. Future applications of both

the protofilament refinement and layer line masking methods will provide further insights into how MAPs, microtubule stabilizing agents, and nucleotide states affect microtubule structure, and how this behavior affects cellular activity as a whole.

Using Cryo-Electron Microscopy to Study Microtubule Heterogeneity

A Dissertation
Presented to the Faculty of the Graduate School
Of
Yale University
In Candidacy for the Degree of
Doctor of Philosophy

By
Garrett Evan Debs

Dissertation Director
Charles V. Sindelar

May 2020

Acknowledgements

I first would like to thank my adviser, Dr. Charles Sindelar for all his help and guidance these past 6 years. I have always felt supported to pursue any avenue of research that I have felt interested in. Even if a project did not work out, Chuck would always offer helpful advice, and was fully supportive of my research changed course. His enthusiasm of research and creative ideas have helped me become the scientist I am today. I would also like to thank my committee members, Drs. Jonathon Howard and Frederick Sigworth for the many helpful suggestions over the past few years. I have been very lucky in having two leaders in their respective fields offer their invaluable insights into my projects.

Next, I would like to thank the members of our lab. In an increasingly collaborative scientific environment, it is very helpful to have people to bounce ideas off of. Furthermore, our lab is an extremely supportive environment where you can both receive troubleshooting ideas, or just complain about what isn't working. Special shoutouts to Kim Gibson for her patience in training me on the microscope. I could only break the vacuum so many times before realizing I must be doing something wrong… A big thanks to Xueqi Liu for being the other 'coder' in the lab. His scripts laid the framework from which I was able to build upon. And a huge thank you to Michael Cha, who collected the majority of the data in this thesis. No one, even you apparently, knows what your special trick is, but I've never seen micrographs as beautiful as yours!

I would also like to thank all of my friends. Graduate school is an extremely stressful time and it is important to have people you feel comfortable spending time around. The late hours of venting, laughing, and playing random (or made up) board games have created memories that I will have with me for life. I realize we are all moving towards a new chapter of our lives, but I know that we will continue to remain friends through it all.

I'd also like to thank my family for always believing in me. My parents have been incredibly supportive throughout my life and I do not know where I would be without them. They have always pushed me to better myself, and most importantly taught me to always be 'true to myself'. They've helped me find my passions and given me the ability to pursue them. This is a privilege not afforded to everyone and I cannot express how grateful I am that they have granted me these opportunities. Also, big thank you to my brother for always being an outlet for extremely interesting conversations that can start and end anywhere. You've always believed me and I've always appreciated it.

Lastly, I'd like to thank my wife, Martha Braun. You've been with me through all the ups and downs and have never wavered in your support or love for me. You've been caring and understanding when I've needed it, but also firm with a strong guiding hand when necessary. You make me want to be a better person, and we both strive to help each other improve. I don't know where I would be without you, and I don't know if I could have finished graduate school without your support. Thank you for help in getting me this far, and I'm very excited to see what life holds for us in this upcoming stage of life. I have to thank the kitties in here somewhere, because that's just what we do, so big thanks to Mr. Kitty and Oscar for keeping the both of us sane.

Table of Contents

Abstract i

Acknowledgements v

Table of Contents vii

Table of Figures ix

Background 1

What are microtubules? A general overview 1

A brief history of microtubule discovery 2

Microtubule Structure 3

Heterogeneity of the microtubule structure 6

Chapter I: Protofilament refinement of Cryo-EM imaged microtubules accounts for inherent disorder in the microtubule wall 9

Introduction 10

Results 15

Protofilament refinement increases the resolution of microtubule reconstructions by correcting for lattice distortions 15

Protofilament subtraction improves upon initial subtraction model 18

Focused 3D classification can be used to identify and reconstruct different subunit types within the microtubule lattice 22

The microtubule wall is flexible 30

The microtubule wall exhibits preferred geometries 31

A shift towards the more curved wall population in Taxol-stabilized microtubules 36

Two distinct wall geometries are associated with two different tubulin m-loop conformations 37
Distortions in the microtubule lattice are local 38
Discussion 42
How stabilizing different wall curvature states could change a microtubule's preferred symmetry type 42
Focused classification allows us to investigate heterogeneous microtubules 44
Methods 46
Chapter II: Alternative cryo-EM methods to study the structure of microtubule-bound spastin. 54
Introduction 55
Results 60
Layer line masking subtracts microtubules prior to refinement 60
Reconstruction of particles from layer-line masked regions 63
Limitations of applying layer-line masking to experimental data 63
Layer line masking successfully subtracts microtubules in experimental data 66
Discussion 67
Methods 70
Appendix I: FSC curves 74
Appendix II: Spastin Purification 76
References 77

Table of Figures

Figure 1: Visual representation of the m-loop 5

Figure 2: Protofilament refinement reconstruction workflow 13

Figure 3: Protofilament refinement of synthetic microtubule images. 14

Figure 4: Protofilament refinement improves the resolutions of microtubule reconstructions. . 20

Figure 5: Protofilament subtraction of a distorted synthetic, microtubule 21

Figure 6: Focused classification of microtubules. 25

Figure 7: Quantification of microtubule distortions. 26

Figure 8: Curve-fitting wall angle distributions for GMPCPP microtubules 27

Figure 9: $\Delta\varphi_M$ plots for individual protofilament pairs corresponding to the leftmost peak in the 13PF GMPCPP seam plot 28

Figure 10: $\Delta\varphi_M$ plots for individual protofilament pairs corresponding to the rightmost peak in the 13PF GMPCPP seam plot 29

Figure 11: Aggregate $\Delta\varphi_M$ distributions for all microtubules in the GMPCPP and Taxol datasets 33

Figure 12: Preferred wall angles are consistent between microtubule symmetry types. 34

Figure 13: Structural differences between the low and high angular states. 35

Figure 14: Autocorrelation of wall angles reveals that distortions in microtubules are local 40

Figure 15: Model of an elemental wall distortion by a protofilament pair 41

Figure 16: Layer line masking workflow 58

Figure 17: Processing results from layer line masking 59

Figure 18: Higher defocus images display clearer spastin density for images with low signal to noise. 61

Figure 19: Poor subtraction of microtubule density following layer line masking. 62

Figure 20: Layer line masking of experimental data yields promising results. 65

Figure 21: FSC curves for the helically and protofilament refined structures for the 14PF GMPCPP and 13PF Taxol sample. 74

Figure 22: FSC curves of remaining mentioned structure 75

Figure 23: SDS PAGE gel of spastin during the different purification steps 76

Background

What are microtubules? A general overview

Microtubules are one of the three main components of the cytoskeleton within Eukaryotic cells. These dynamic, filamentous polymers play extremely diverse roles in the cell, such as mitosis (Prosser and Pelletier, 2017) and intracellular transport mediated by molecular motors (Howard, 1997). Understanding the role of microtubules and the associated proteins in these processes has led to many different vibrant fields of research for over half a century.

Microtubules consist of α/β-tubulin heterodimers that polymerize longitudinally in the presence of GTP to form protofilaments and interact laterally to form microtubules (Conde and Caceres, 2009). In general, lateral interactions are mediated by 'B-lattice' type interactions, wherein α and α-tubulin will interact and β and β-tubulin will interact. However, there is a disruption in the helical symmetry of the microtubule wherein an 'A-lattice' type interaction will occur, with α and β-tubulin interacting laterally. This site of symmetry disruption is known as the seam (Kikkawa et al., 1994). Because of microtubule's cylindrical symmetry, but not quite helical symmetry due to the disruption at the seam, microtubules are frequently referred to as pseudo-helical.

In general, microtubules will consist of 13-protofilaments, however, different factors can affect the number of protofilaments in a microtubule (Andreu et al., 1992; Tilney et al., 1973). Microtubules are dynamic polymers that can rapidly switch from elongating to shrinking and back again; a property called dynamic instability. Hydrolysis of GTP is proposed to play a key role in dynamic instability (Mitchison and Kirschner, 1984). Regulation of these microtubule dynamics is essential, as dynamic microtubules participate in numerous cellular processes (Brouhard and Rice, 2018).

A brief history of microtubule discovery

Although biophysical evidence of microtubules has existed as far back as 1939, microtubules hadn't been well visualized until the mid-1950s (Brinkley, 1997). Using electron microscopy (EM), cilia of different organisms were observed to consist of tubular structures (Fawcett and Porter, 1954; Manton and Clarke, 1952). However, observations of these structures were limited due to poor sample fixation (Brinkley, 1997). With the advent of improved fixation in 1963, Ledbetter and Porter were better able to observe these structures in variety of different plant cells and named them microtubules (Ledbetter and Porter, 1963). Importantly, they also noted that these ever-present tubular structures were identical to the tubules seen at the mitotic spindles. This observation was important because it was already known that animal cells also contained tubular filaments in their mitotic spindles (Harris, 1962). These observations hinted at the importance of these structures and their possible ubiquity in eukaryotic cells.

Shortly after microtubules as macromolecular complex had been discovered, the overall structure began getting broken down into smaller components. Continuing the run of discoveries following better visualization due to improved EM staining techniques, it was noted that microtubules consisted of 'filamentous subunits', or protofilaments (Ledbetter and Porter, 1964; Pease, 1963). Shortly afterwards, Edwin Taylor's lab began a series of biochemical experiments using colchicine (which was known to disrupt mitosis and the mitotic spindle structure (Borisy and Taylor, 1967a)) as a marker to identify and isolate what we know now as a tubulin heterodimer (Borisy and Taylor, 1967a, b; Shelanski and Taylor, 1967). In 1971, Bryan and Wilson showed that this fundamental microtubule building block, is actually a heterodimer composed of two separate proteins (Bryan and Wilson, 1971), the α and β tubulin subunits.

Microtubule Structure

Studying the structure of microtubules has always been a challenge. Because microtubules are polymers, forming crystals with their fundamental subunits (i.e. a tubulin heterodimer), is extremely difficult. This means that x-ray crystallography of tubulin is challenging. Additionally, until recently, electron microscopy (EM) was technically challenging and was mostly useful for solving low resolution structures. Nevertheless, the race to solve the first high resolution structure of tubulin began. The beginning of the race was dominated largely by EM. As already noted above, microtubules were first discovered and much of the core structure was determined using EM in the early 1960's. Another structural breakthrough came when researchers discovered that polymerization of tubulin in the presence of Zn^{2+} led to the formation of sheets of protofilaments, rather than closing and forming microtubules (Larsson et al., 1976), leading to a 20 Å reconstruction of a the protofilaments (Amos and Baker, 1979). X-ray fiber diffraction marginally improved this resolution several year later (Beese et al., 1987).

A big breakthrough in solving a high-resolution structure of tubulin occurred in 1995 in Ken Downing's lab. Using Taxol stabilized, zinc-induced crystalline sheets, a 6.5 Å structure of tubulin had been solved using electron crystallography, and the Taxol-binding site was found to be located specifically on β-tubulin (Nogales et al., 1995). Note, Taxol was, and is, an important microtubule binding molecule as it stabilizes microtubules and is an anti-cancer drug (Dumontet and Jordan, 2010). This seemed to be the breakthrough necessary as only a few short years later, the first atomic structure (3.7 Å) of tubulin was solved from the same lab and technique, except using cryo-EM images instead of negatively stained micrographs. This structure provided important insights into the structural basis of nucleotide exchange, showing that each tubulin subunit binds to a GTP molecule at the interaction interface with other the tubulin subunits. Thus, the GTP bound α tubulin is located at the heterodimer interface and is essentially permanently

bound at this non-exchangeable site. Conversely, GTP bound to β tubulin is buried at the dimer-dimer interface, but is exposed when not polymerized. Because these zinc-induced sheets contained anti-parallel protofilaments (in contrast to the parallel arrangements of protofilaments found in microtubules), only important longitudinal contacts could be determined from this structure (Nogales et al., 1998). However, docking of atomic maps of individual protofilaments into low resolution microtubule structures allowed for identification of key lateral contacts between protofilaments within a microtubule. Most notably, the m-loop of tubulin was seen to be an important point of contact between protofilaments (Nogales et al., 1999). Shortly afterward, an 8 Å structure was solved using cryo-EM of microtubules, and a fairly modern reconstruction algorithm. This structure was more accurate than the atomic, protofilament model docked into a low resolution microtubule structure, and also elucidated the importance of the m-loop in lateral interactions between protofilaments (Li et al., 2002).

While structural advances using EM were occurring, there was progress solving the tubulin structure as well. Previously, crystal structures of actin, another filamentous polymer, were made possible by co-crystallization of a polymerization inhibitor (Kabsch et al., 1990). In a similar manner, the structure of tubulin could be solved. In 2000, a 4 Å X-ray structure of tubulin bound to a microtubule depolymerizer was solved (Gigant et al., 2000). While this structure is at lower resolution that structures of tubulin solved using EM, the utility of this structure lies in that shows and important intermediate of the depolymerization process.

The mid 2000's and early 2010's was full of microtubule structures being solved to moderate resolution using cryo-EM. The importance of most of these structures were mostly derived from the microtubule binding protein that the microtubules were frozen with (Sindelar and Downing, 2007, 2010; Sui and Downing, 2010).

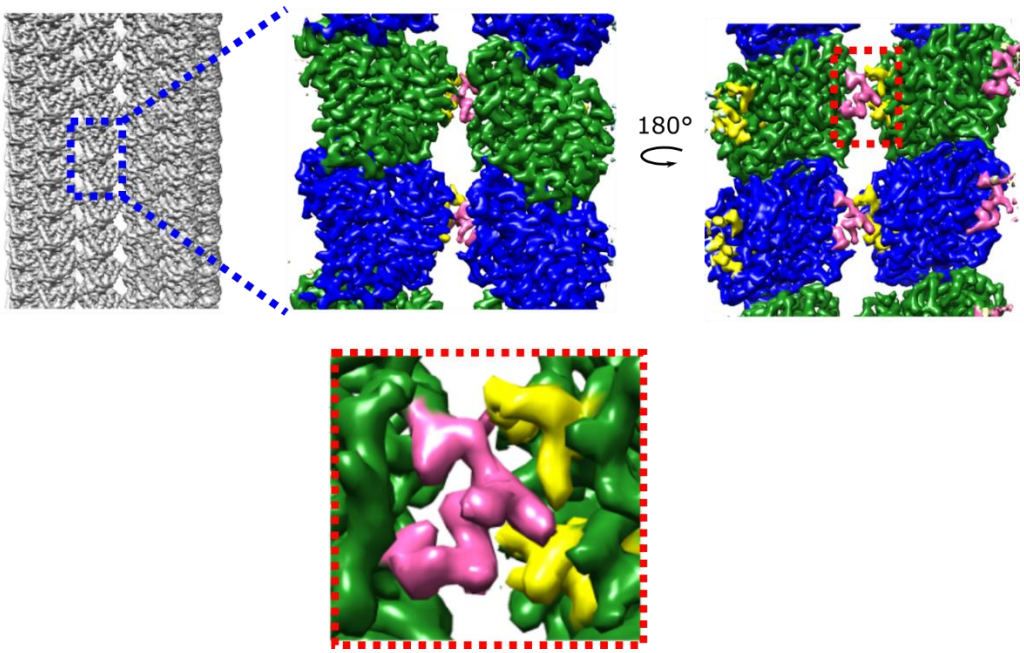

Figure 1: Visual representation of the m-loop. A 3D reconstruction of a microtubule (left). Zoomed view of two neighboring tubulin dimers, with the α-tubulin in green, and β-tubulin in blue (middle). Same two tubulin dimers, as viewed from the lumen of the microtubule. The m-loop is colored pink, and the H1'-S2 and H2-S3 loops are colored yellow (right). Zoomed in view of the 'lock and key' configuration of the m-loop and associated loops. Displayed reconstructions are from data discussed below.

Along with the rest of the cryo-EM world, the field of microtubule structure massively benefited from the advent of direct electron detectors. A series of sub 4 Å and 5 Å structures from the Nogales lab revealed important structural information regarding lateral contacts between protofilaments, as well as structural insights of microtubule dynamics (Alushin et al., 2014; Zhang et al., 2015). While previous structures had shown the importance of the m-loop in lateral contacts, these structures were the first to directly show the m-loop of one tubulin subunit, and the H1'-S2 and H2-S3 loops of the adjacent subunit interacting in a 'lock and key' configuration (Figure 1). Typically, H283 from the α-tubulin m-loop will be positioned between the H1'-S2 and H2-S3 loops of the adjacent α-tubulin, and Y283 from the β-tubulin m-loop will interact similarly with the adjacent β-tubulin (Zhang et al., 2015). Furthermore, these recent structures have led to the 'lattice compaction' model, which proposes a mechanism by which microtubules are destabilized by the hydrolysis of GTP. First, hydrolysis of GTP leads to compaction of the dimer-dimer interface (Alushin et al., 2014; Zhang et al., 2015). In addition to compaction of the lattice, hydrolysis also leads to a negative rotation in the supertwist of the microtubule lattice. Following release of the inorganic phosphate, there is a positive rotation in the supertwist, that almost returns the lattice twist to the original value (Zhang et al., 2018). While these structures have proven invaluable to the field, there has always been one glaring oversight in study of microtubule structure: the assumption of pseudo-helical symmetry.

Heterogeneity of the microtubule structure

Interestingly, while the above structures are reported using helical symmetry during cryo-EM refinement, some of these recent structures have noted a distortion occurring at the microtubule seam (Kellogg et al., 2017; Zhang et al., 2015; Zhang et al., 2018). Notably, under different biochemical conditions, an ~3° outward rotation is observed between the corresponding protofilaments. Nevertheless, this distortion is largely ignored when pseudo-helical symmetry is

applied and structural information is parsed from the resulting volumes. More recently, it has been observed that microtubules frequently distort, and full reconstructed volumes yielded from 3D classification of microtubules reveal what look like 'squashed' microtubules (Lacey et al., 2019). Furthermore, a comprehensive structural study of microtubule stabilizing drugs showed that while some drugs increase the structural homogeneity of the microtubule lattice, others make the lattice less structurally coherent (Kellogg et al., 2017). These results strongly suggest that microtubules may be distorted under commonly studied biochemical conditions, and analyzing and understanding this behavior may be important for understanding microtubule behavior.

In addition to structural heterogeneity inherent to the microtubule due to flexibility of the lattice, microtubules can also differ based on the number of protofilaments. Typical *in vitro* polymerized microtubules will contain 11-16 protofilaments (Manka and Moores, 2018). However, 13 protofilament microtubules are typically found in cells (Tilney et al., 1973), although this may not always be the case (Chaaban and Brouhard, 2017). To explain the disparity between the protofilament number *in vitro* and *in vivo*, it has been shown that various microtubule binding drugs, proteins, and even tubulin isoforms can affect the average number of protofilaments in a microtubule (Andreu et al., 1992; des Georges et al., 2008; Diaz et al., 1998; Moores et al., 2004; Ti et al., 2018). Interestingly, microtubules with different numbers of protofilaments were observed to have different distortions at the seam, even under the same biochemical conditions (Zhang et al., 2018). Given the postulation that this distortion at the seam could be a weak point in a microtubule, and might be the origin of depolymerization, understanding the correlation between protofilament number and distortion in the microtubule lattice will be key.

A final layer of heterogeneity discussed in this thesis will be that of irregularly bound proteins. Studies of microtubule binding proteins that are not fully decorating the surface of

microtubules may be desirable in order to find that protein in different structural states. For instance, studying a kinesin dimer bound to microtubules will need a method to distinguish the two different bound heads. If there is no distinction, the two structural states will be averaged together and no new information can be obtained (Liu et al., 2017). Our lab has previously addressed this issue using FINDKIN, a template searching method that identifies locations where proteins are bound. However, improvement of this method is possible, especially if proteins are significantly larger than a tubulin dimer. Cryo-EM methods capable of reconstructing such datasets would open the door to structural studies of various microtubule binding proteins.

Here I will present three new methods for studying heterogeneity within microtubules using cryo-EM. The first will address the issue of microtubule distortions, and the second two will focus on solving the structure of microtubule binding proteins. Additionally, using results from these new techniques, I will analyze microtubules distortions and derive a model of what the cross-section of a microtubule actually looks like.

Chapter I: Protofilament refinement of Cryo-EM imaged microtubules accounts for inherent disorder in the microtubule wall

Contribution statement: Michael Cha collected all the micrographs discussed in this chapter. Dr. Xueqi Liu wrote the smoothing scripts that are used. Professor Charles Sindelar wrote the scripts to generate synthetic microtubule images. Together, Professor Sindelar and I analyzed and interpreted the results.

Introduction

While microtubules have generally been thought of as symmetric tubes, recent 3D cryo-electron microscopy (cryo-EM) reconstructions of these structures have presented evidence suggesting that this is not always the case. This poses a problem for structural studies of microtubules, as conventional microtubule reconstruction methods assume near helical symmetry (Sindelar and Downing, 2007; Zhang and Nogales, 2015). Any deviation from helical symmetry in the imaged microtubules will be lost in the averaged microtubule structure, as well as decrease the overall resolution and quality of the 3D reconstructed map. While 3D classification of the microtubule particles has yielded different 'squashed' classes of microtubule volumes, the overall quality of these maps did not increase (Lacey et al., 2019), suggesting there is still a lot of inherent heterogeneity in the microtubule structure that is not captured in these classified volumes.

A method capable of aligning portions of the microtubule wall rather than full microtubule cross-sections is necessary to account for distortions within the microtubule lattice. The limit of conventional microtubule refinement methods lies in the fact that full microtubule segments are aligned and averaged together to reconstruct the final volume. If there are any distortions in the microtubule cross-section, then there is an alignment error that cannot be corrected for using traditional techniques. However, by aligning only one protofilament at a time, there are more degrees of freedom during refinement, which allows for a more accurate measurement of the protofilaments location within the microtubule. Ultimately this will lead to a

higher quality reconstruction of the tubulin dimers that make up a microtubule. Additionally, the resulting alignment parameters can be utilized to gain insights into what individual microtubule cross-sections actually look like.

Note that distinguishing between α and β-tubulin subunits within imaged microtubules is challenging due to their high structural similarity, and failure to do so causes the two to be averaged together during helical refinement. While this problem has been previously addressed, the existing methods rely on the assumption that each microtubule has only one seam. Previous results have shown that this is not always the case (des Georges et al., 2008; Kikkawa et al., 1994). However, by focusing on determining the α/β-register of each protofilament one at a time, you can remove the assumption that the microtubule only has one seam. Thus, the resulting method would allow for multi-seamed microtubules to be correctly aligned.

Reconstruction of microtubules containing cofactors with incomplete or mixed occupancies within the microtubule lattice has proven to be a challenging problem (Liu et al., 2017). The issue is that averaging microtubule segments with different cofactor states will result in a smeared average of binding site. For example, if we're studying a kinesin dimer that binds irregularly to the lattice, conventional microtubule reconstruction methods will result in a smeared average of all the bound states. The unbound sites will be averaged with the bound sites, and both heads of kinesin dimer will also be averaged together, resulting in a structure with no interpretable kinesin density (Liu et al., 2017). In principle, classification can handle these issues by discriminating between different structural states of an image segment. However, when there are many independent filament subunits per image segment (~100 tubulin dimers per microtubule image segment) the corresponding number of classes becomes prohibitive (i.e. n^{100} classes for n distinct states per subunit). However, by continuing the idea of focusing on a smaller portion of the microtubule segment at one time, classification of a single tubulin subunit makes

the problem much more manageable. Here I present my 'protofilament refinement' method that allows for accurate alignment of distorted microtubule and focused classification of protofilaments to find the α/β-register as well bound and unbound kinesin sites. Additionally, the alignment parameters resulting from use of this method are further analyzed in order to gain insights into the dynamic behavior of lateral protofilament interactions.

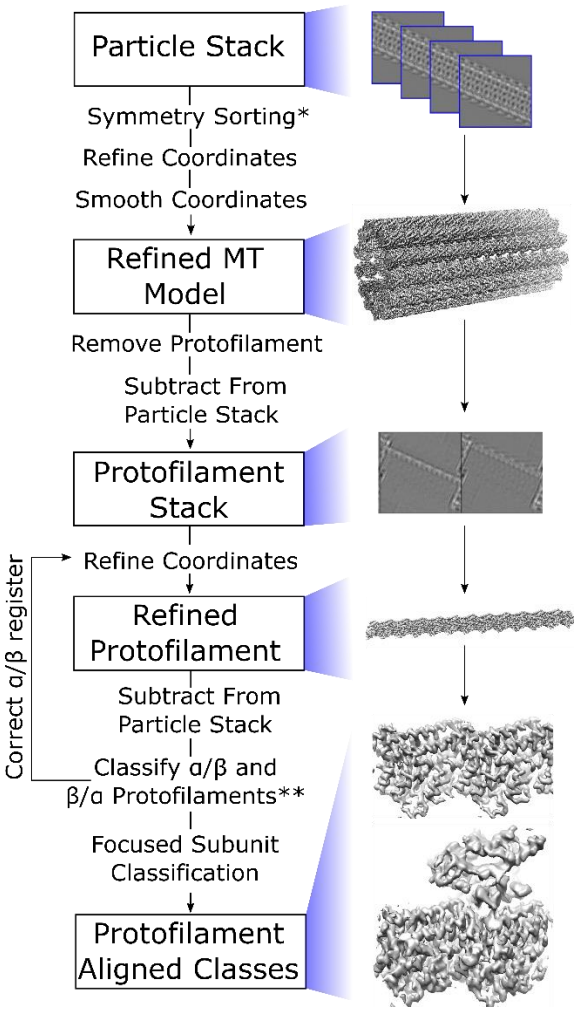

Figure 2: Protofilament refinement reconstruction workflow that allows for correction of lattice distortions and single subunit classification. Microtubules particles are first sorted based on their symmetry type and the coordinates are refined and smoothed to fit the expected helical geometry. A protofilament is removed from this model and used to subtract from the initial particle stack in order to generate a stack of protofilament particles. These protofilament particles are then refined. The protofilament coordinates are used for a second round of improved subtraction in order to generate a second stack of protofilament particles. These are then classified in order to determine the register of the α and β tubulin. The protofilament coordinates are corrected in order to put all protofilaments in the correct register and the protofilament particles are refined again. Following the second refinement, potential protein binding sites are classified in order to reconstruct their density as well.

* If microtubule is fully decorated with kinesin, the seam is determined at this step.

** Once the seam(s) has been found, proceed to focused subunit classification.

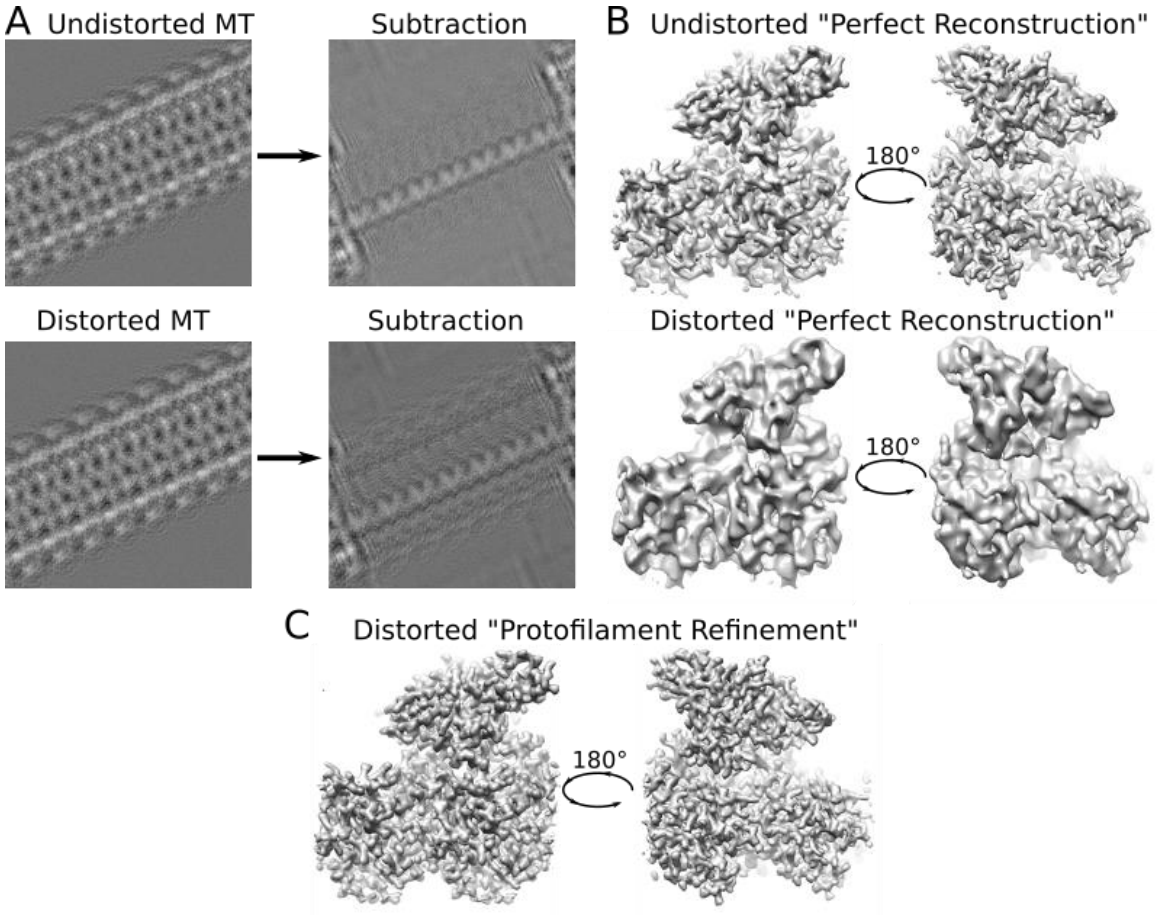

Figure 3: Protofilament refinement of synthetic microtubule images. (*A*) Subtraction of microtubule model with missing protofilament for an undistorted (top) and distorted (bottom) microtubule image. (*B*) Representative tubulin dimer with bound kinesin from the reconstruction of microtubule particles using the 'perfect' alignment parameters for undistorted (top) and distorted (bottom) microtubule images. (*C*) Representative tubulin dimer with bound kinesin from the final reconstructed volume following protofilament refinement.

Results

Protofilament refinement increases the resolution of microtubule reconstructions by correcting for lattice distortions

To overcome challenges associated with refining 3D structures from cryo-EM images of distorted microtubules, I developed a pipeline to align individual protofilaments within the imaged microtubules (Figure 2). First, previously established methods for microtubule symmetry sorting and helical processing are applied to microtubule image segments to obtain an initial 3D reconstruction of the intact microtubule. Briefly, selected microtubule particles are first sorted into their respective symmetry types as determined by the number of protofilaments. Next, asymmetric, high-resolution 3D refinement is performed in order to obtain a reconstruction of the microtubule volume. Euler angles corresponding to the refinement are then 'smoothed' in order to ensure continuity of the alignment parameters for each segment in a microtubule. Smoothing ensures that phenomena like polarity switching does not occur between neighboring segments of a microtubule. Finally, Euler angles corresponding to the smoothed microtubule particles are used to generate a volume for use in later processing steps.

Using this microtubule volume, masked signal subtraction is then performed to erase all but a single protofilament in each microtubule segment. This process is repeated for each protofilament in a given microtubule segment, resulting in *N* times more segment images (where *N* corresponds to the number of protofilaments for a given microtubule symmetry type). The resulting 'protofilament particles' are then further refined as single particles. This 'protofilament refinement' method increases *N*-fold the number of degrees of freedom explored compared with the original microtubule refinement, thus enabling deviations from helical symmetry to be explicitly accounted for and corrected. Note that there may be additional classification steps necessary if the seam has not been found and/or there is heterogeneity on the surface on the microtubule. These steps will be discussed later.

Application of the protofilament refinement method to synthetic images generated from asymmetrically distorted, microtubule atomic models yielded substantial gains in the quality of the reconstructed maps, compared with conventional helical processing (Figure 3). The cross-section of synthetic microtubule models was randomly perturbed to vary the aspect ratio (ie: distort/squash the microtubule cross-section). These models were projected using randomized Euler angles to produce a series of synthetic micrographs. Protofilament refinement of the resulting synthetic, distorted-microtubule images yielded a 3D map where all features, including side-chains, were resolved to the Nyquist frequency (~2.5 Å resolution). This volume is essentially indistinguishable from the map obtained by refining a corresponding set of synthetic, undistorted-microtubule images. In contrast, conventional helical processing of the synthetic, distorted-microtubule images yielded 3D maps without visible side-chain densities and poorly resolved secondary structural elements. Because synthetic images were used, the 'perfect' helical alignment parameters could also be used to reconstruct the microtubule volume for the distorted microtubule images. This volume was also poorly resolved.

In addition to refining the microtubule one protofilament at a time, a 3x3 'patch' of tubulin dimers (ie: 3 tubulin dimers from 3 adjacent protofilaments for a total of 9 dimers) was also refined. The idea was that the patch of tubulin dimers may have a stronger signal since a protofilament is so thin, and thus there may be benefit in refining a patch over a protofilament. However, while refinement of the patch yielded tubulin density that looked significantly better relative to the final helical refinement volume, the tubulin volumes throughout the patch looked different relative to one another. While tubulin from one protofilament looked like they had been resolved near the Nyquist frequency, dimers from another protofilament were more smeared. This result suggests that refinement of a 3x3 patch of tubulin dimers is not capable of capturing the behavior of the microtubule wall. For this reason, a protofilament segment was determined

to be the better starting model. Note, that protofilament segments are ~7 tubulin dimers in length, and shortening the protofilament segment did not improve 3D refinement.

Application of protofilament refinement to experimentally imaged microtubules further demonstrated the ability of the method to better resolve high-resolution features. Two sample types with distinct compositions were analyzed: GMPCPP stabilized microtubules fully decorated with monomeric kinesin motor domains, and a more heterogenous sample containing Taxol stabilized microtubules sparsely decorated with dimeric kinesin motor domains. For the GMPCPP sample, helical refinement of 14-protofilament microtubules (the predominant symmetry type with this nucleotide analog) yielded a map with an estimated resolution of 4.1 Å using ~400K tubulin dimers (Figure 4A). Note that this resolution is worse than was reported for several previous cryo-EM analyses of GMPCPP-microtubule structures that used similar numbers of particles, which may reflect intrinsic heterogeneity associated with the kinesin nucleotide state found in our sample. Moreover, anisotropic blurring is evident in many regions of the volume, particularly within the kinesin region where β-sheet strands are not resolved. Following protofilament refinement, map resolution is substantially improved (3.6 Å overall), anisotropic blurring is no longer evident, side-chains are well resolved throughout most of the map, and the kinesin backbone is nearly entirely traceable.

Applying protofilament refinement to the Taxol sample similarly resulted in pronounced gains in map quality. For 13-protofilament, Taxol-microtubules (the more populated symmetry type with this stabilizing drug), helical refinement yielded a map with an estimated resolution of 3.3 Å using ~550K particles (Figure 4B). Similar to the GMPCPP sample, the helically refined Taxol structure shows pronounced anisotropic blurring. Despite the improvement in estimated resolution relative to the helically refined GMPCPP map, the Taxol map is not significantly more detailed. Following protofilament refinement, the Taxol map resolution improved to 2.9 Å,

anisotropic blurring is no longer evident, and side-chains are clearly resolved throughout the map. While we attribute most of these gains to improved particle alignments, the protofilament refined map also benefitted from an increased number of particles compared with the helical refinement (~850K vs ~550K). This increase in particle number is due to the inclusion of multi-seamed microtubules during protofilament refinement, made possible by the additional classification step described below. Because conventional helical processing cannot correctly align multi-seamed microtubules, they were excluded from the helical refinement. These results demonstrate that protofilament refinement has the potential to improve the resolution of microtubule images under a number of different conditions.

Protofilament subtraction improves upon initial subtraction model

Protofilament refinement increased the resolution of 3D refinements because distortions in a microtubule cross-section can be accounted for. This statement is supported by the increase in resolution of a tubulin subunit within the microtubule structure following protofilament refinement. (While this is currently the only supporting evidence presented, I will later show more compelling evidence. However, for the purposes of discussing this next section, this evidence will suffice). Because protofilament refinement significantly improves refinement quality of reconstructed maps, it's safe to say that, on average, the majority of the microtubules in the sample are at least somewhat distorted. Thinking back to the initial microtubule subtraction step, symmetric microtubule volumes were used to generate our protofilament particles. However, if the majority of microtubules are distorted, then we know that this initial subtraction step must be poor due to the bad subtraction volume. However, following protofilament refinement, we have a more accurate representation (on average) of each protofilament in our entire dataset. Thus, rather than using a symmetric microtubule volume and corresponding

symmetrized microtubule Euler angles for the subtraction step, a protofilament volume and the refined protofilament Euler angles can be used for the subtraction step.

'Protofilament subtraction' is performed by using both the volume and Euler angles resulting from protofilament refinement. Subtraction is performed sequentially on *N*-1 protofilaments in each microtubule particle so that the resulting particle only contains one protofilament. This is done for each protofilament a given microtubule particle. Comparing images of protofilament particles resulting from subtracting a microtubule model with protofilament particles resulting from protofilament subtraction reveals that there is less residual density following protofilament subtraction (Figure 5). Additionally, comparison of volumes resulting from reconstruction of the protofilament particles reveals that there is less residual density outside the protofilament of interest for particles that have undergone protofilament subtraction relative to microtubule subtraction. All these data suggest that protofilament subtraction is more accurate due to the ability to account for microtubule distortions.

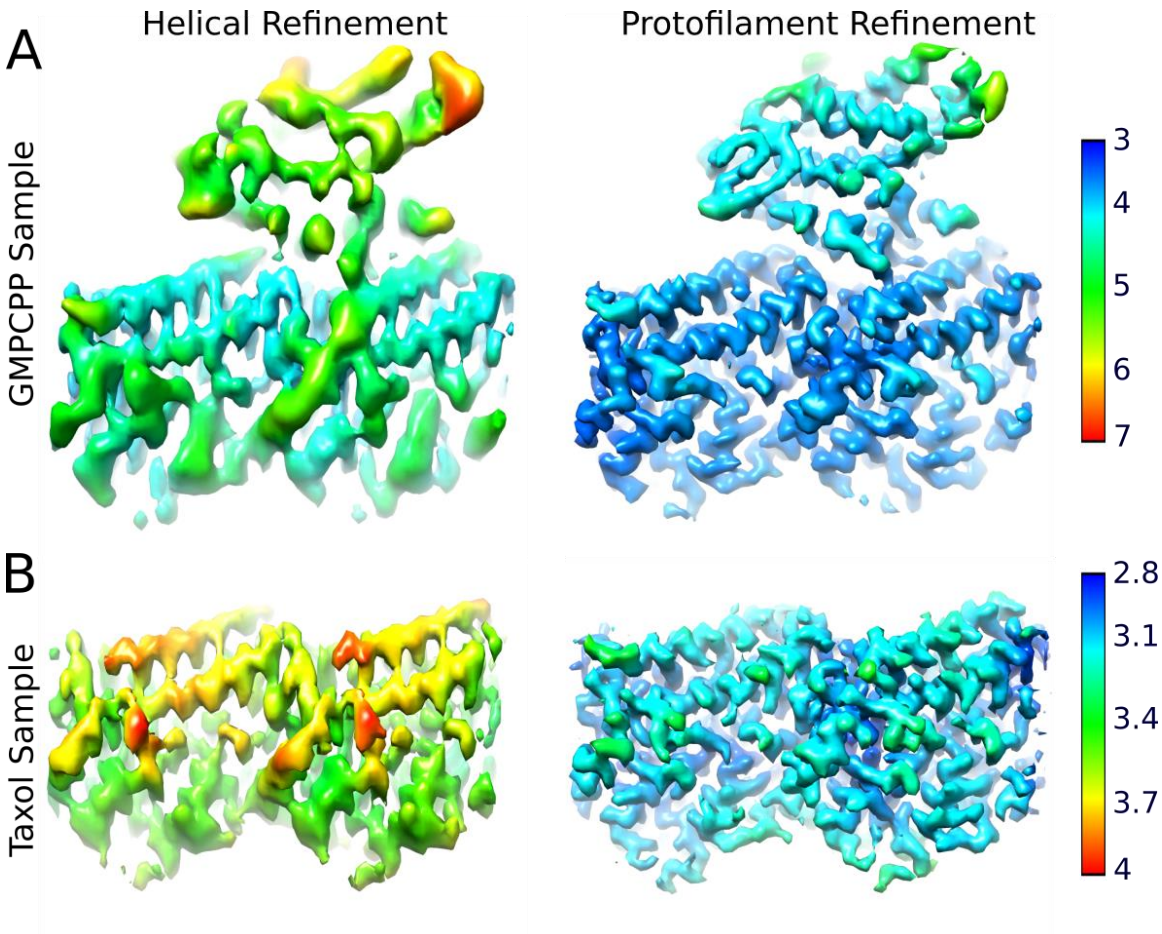

Figure 4: Protofilament refinement improves the resolutions of microtubule reconstructions. (*A*) Local resolution of a 14-protofilament, GMPCPP-stabilized microtubule, fully decorated with kinesin. The left represents the reconstruction following traditional microtubule refinement methods and the right is the structure following protofilament refinement. (*B*) Local resolution of a 13-protofilament, Taxol-stabilized microtubule sparsely decorated with kinesin. Due to low kinesin density, the overall refinement does not have a visible kinesin signal at this threshold. 3D classification can be used to find and reconstruct kinesin bound sites as shown in Figure 3**.** The local resolution was calculated using BSoft using a 0.5 FSC cutoff. Note the difference in scale bars between A and B.

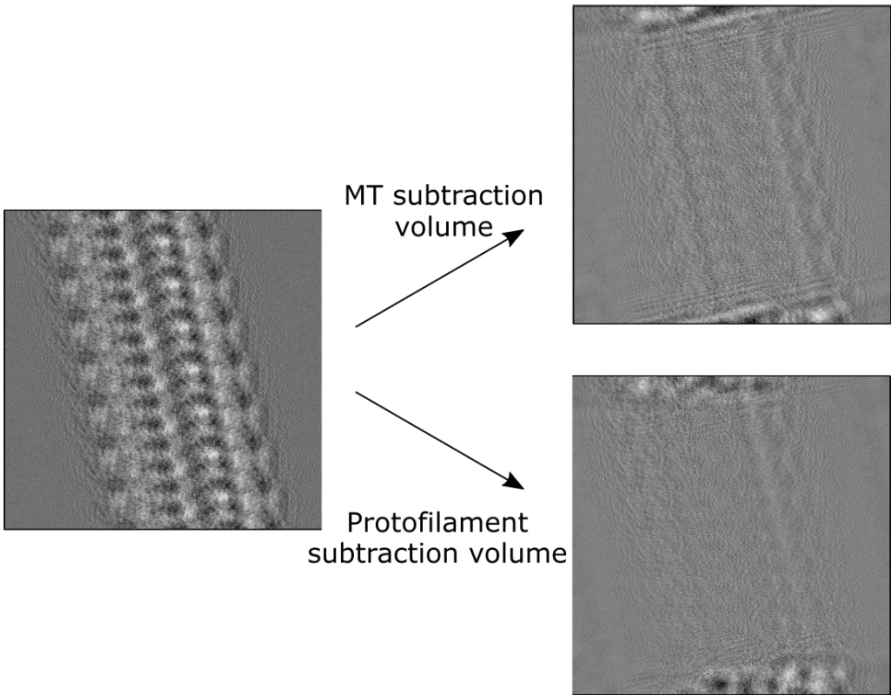

Figure 5: Protofilament subtraction of a distorted synthetic, microtubule. Following subtraction using a full microtubule volume (top) there is a lot of residual density. However, following protofilament subtraction (bottom), a lot of this residual density is removed.

Focused 3D classification can be used to identify and reconstruct different subunit types within the microtubule lattice

Following protofilament refinement, an accurate representation of each tubulin dimer in each dataset is obtained, thus the problem of heterogeneity within the sample can be addressed. First, in the previous section I glossed over how to distinguish between α and β-tubulin for samples without protein biomarker (such as kinesin). Additionally, for datasets containing incomplete kinesin decoration (or any other occupying cofactor), I would like to be able to determine where kinesin is located. I therefore adopted a focused classification strategy (Bai et al., 2015), where filament segments are divided into subregions, such as individual tubulin dimers and protein cofactors, that are treated separately (Mentes et al., 2018). In this way, classification can be used to discriminate between features such as α and β tubulin or occupying cofactors one subunit at a time. To apply this strategy to microtubule samples, we selected a region of interest within the microtubule structure, and signal outside this region was subtracted from the original particle images; the resulting particles, containing mostly signal from the region of interest, were then subjected to 3D classification without alignment.

First, α and β-tubulin in the Taxol dataset were distinguished by focusing classification on a single protofilament, using the particles resulting from protofilament subtraction. Prior to classification, inability to discriminate α vs β-tubulin suggests that any given protofilament could be offset from its correct position (referred to as 'α/β-register') by ~40 Å (referred to as 'β/α-register'). Initial efforts to sort these two registers into distinct classes, using a random initialization to seed the classes, gave rise to a single dominant class that lacked any distinct α vs β-tubulin features. The classification was therefore seeded with synthetic maps generated from α/β-register and β/α-register protofilament atomic models. The resulting class assignments unambiguously established the register of each protofilament in ~60% of the microtubules. The remaining microtubules were excluded from further analysis. Coordinates of protofilaments that

were classified to be in the β/α-register were shifted by ~40 Å along the microtubule axis, thereby aligning all protofilaments to a common register.

Interestingly, this α/β-tubulin classification procedure not only determined the seam orientations in imaged microtubules, but also identified a substantial population of multi-seamed microtubules (Figure 6A-C). Our method identified multiple seams in ~36% of the analyzed 13-protofilament microtubules and ~10% of the analyzed 12-protofilament microtubules. To validate this finding, microtubule particles containing two adjacent seams were used to generate a 3D reconstruction, which exhibited the expected protofilament register pattern (Figure 6B). This multi-seamed property of Taxol microtubules evidently did not extend to GMPCPP samples; only one of the 270 analyzed microtubules had an additional seam.

Following protofilament register assignment, a second round of focused classification was used to identify bound kinesin sites within the Taxol sample. To maximize signal and increase the resolution, an additional round of protofilament refinement was performed prior to this classification step. A region of interest enveloping the kinesin binding site was the locus for reference-free focused classification with *n=2* classes. Classification failed to converge using default classification parameters (i.e. all ~850K subunits were included in the classification and seeded by a random initialization), with class populations exhibiting unstable behavior over many iterations. However, if the classification was restricted to a small random subset of our data (~25K subunits), the procedure consistently converged to two classes: (1) a bare tubulin class, and (2) a class exhibiting a bound kinesin motor domain. These two classes could then be used to seed a classification of the entire dataset, resulting in a bare tubulin class with ~730K particles and a kinesin class with ~120K particles. Further analysis and physiological implications of these results are discussed extensively in Michael Cha's thesis and thus won't be reiterated here.

While these results show that a combinatorial approach of protofilament refinement and focused classification can yield high resolution structures of protofilaments and irregularly bound protein, it's important to note that the in order which these techniques are applied is important. If focused classification is performed prior to protofilament refinement, the resulting classes appear to differ based on locational translation, not structural heterogeneity. Using an example of finding bound kinesin motors, focused classification doesn't result in a bare tubulin class and a kinesin motor if protofilament refinement has not been performed. Instead, vertical translations of otherwise identical classes are observed. This result highlights the inherent disorder in a microtubule lattice, and the necessity to correct these distortions during Cryo-EM refinement. Furthermore, this result could also explain why identifying the locations of bound protein has proven difficult in the past.

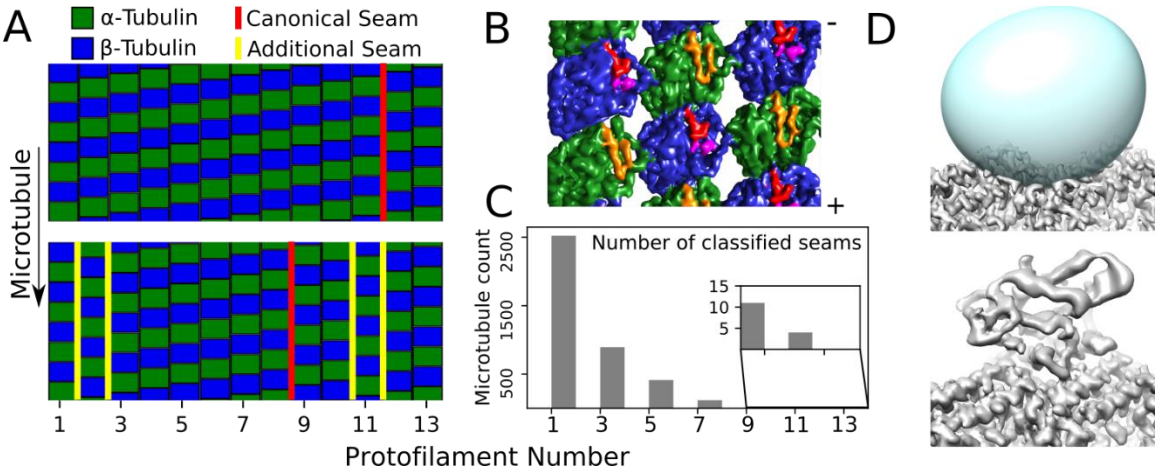

Figure 6: Focused classification of microtubules. (*A*) Classification results for a single seam microtubule (top, marked in red), and a five-seam microtubule (bottom). Two protofilaments in the five-seam microtubule are out of register resulting in four additional seams (marked in yellow). (*B*) Lumen view of a microtubule reconstruction centered on an out of register protofilament illustrating the two additional seams created. α-tubulin is colored green with the S9-S10 loop colored orange, while β-tubulin is blue with the S9-S10 loop in red and Taxol in purple. (*C*) Quantification of the number of microtubules that have additional seams. (*D*) Classification of the kinesin binding site. The predicted binding location is masked (top, mask in cyan) and the remaining tubulin density is subtracted away. Classification results in bound (bottom) and unbound (not displayed) states.

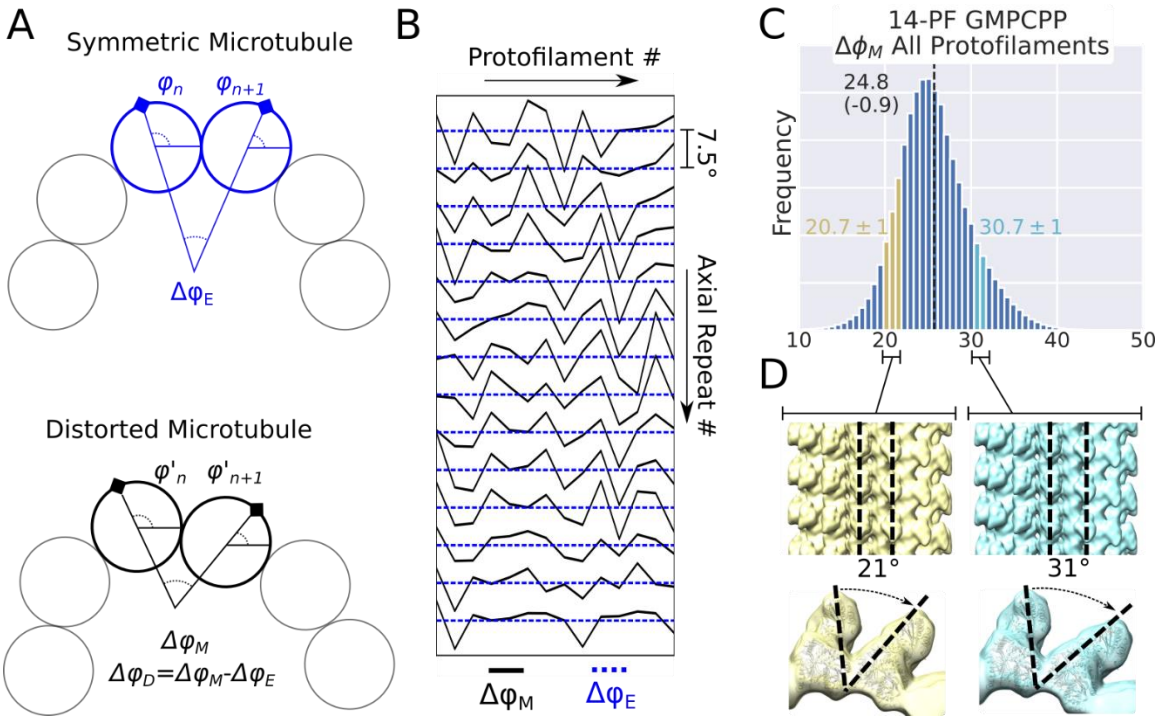

Figure 7: Quantification of microtubule distortions. (*A*) Illustration of the expected rotation difference between neighboring filaments ($\Delta\varphi$) in a symmetric microtubule (top, $\Delta\varphi_E$) and in a distorted microtubule (bottom, $\Delta\varphi_M$). (*B*) $\Delta\varphi_M$ for a representative microtubule, plotted as a function of protofilament number (x-axis) and axial repeat number (y-axis). $\Delta\varphi_E$ is plotted in blue as a reference and each axial repeat is spaced by 7.5°. (*C*) A histogram of $\Delta\varphi_M$ values for all the microtubules in the 14-protofilament GMPCPP-microtubule dataset. The dashed, black line denotes $\Delta\varphi_E$ for a 14-protofilament microtubule. Particles corresponding to the highlighted $\Delta\varphi_M$ values were selectively reconstructed (D), yielding angles of 21° and 31° between the target protofilaments.

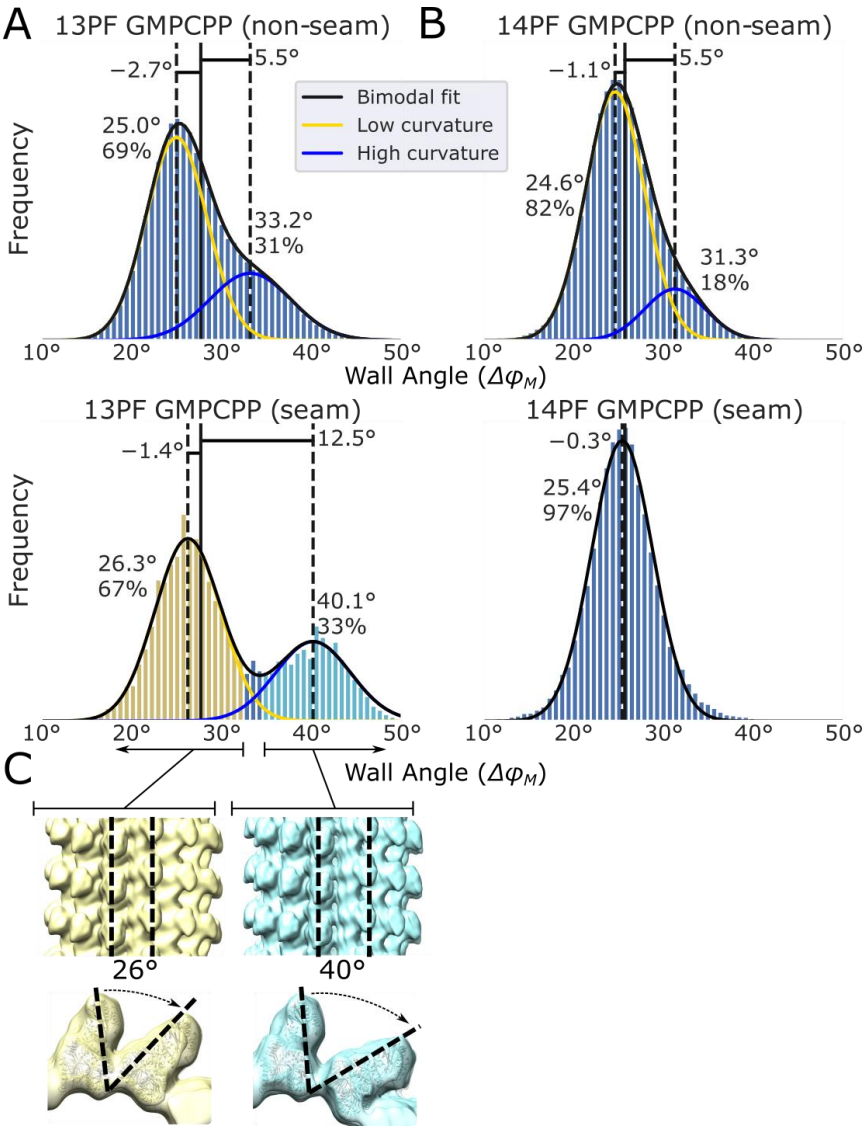

Figure 8: Curve-fitting wall angle distributions for GMPCPP microtubules reveals bimodal behavior of the wall geometries. (*A*) Histogram of wall angles corresponding to non-seam (top) and seam (bottom) protofilaments for a 13-protofilament GMPCPP-microtubule. These distributions have been fit by a double gaussian curve, with each peak's mean and relative population noted by the respective peaks. The distance of each peak from the symmetric wall angle ($\Delta\varphi_E$, denoted by the solid black line) is also noted above each peak. (*B*). Histogram of wall angles corresponding to non-seam (top) and seam (bottom) protofilaments for a 14-protofilament GMPCPP-microtubule. The non-seam angles were fit to a double gaussian whereas the seam angles were fit to a single gaussian curve. (*C*) Particles corresponding to the angles in each peak of the bottom histogram in (*A*) were selectively reconstructed to visualize the two distinct seam populations.

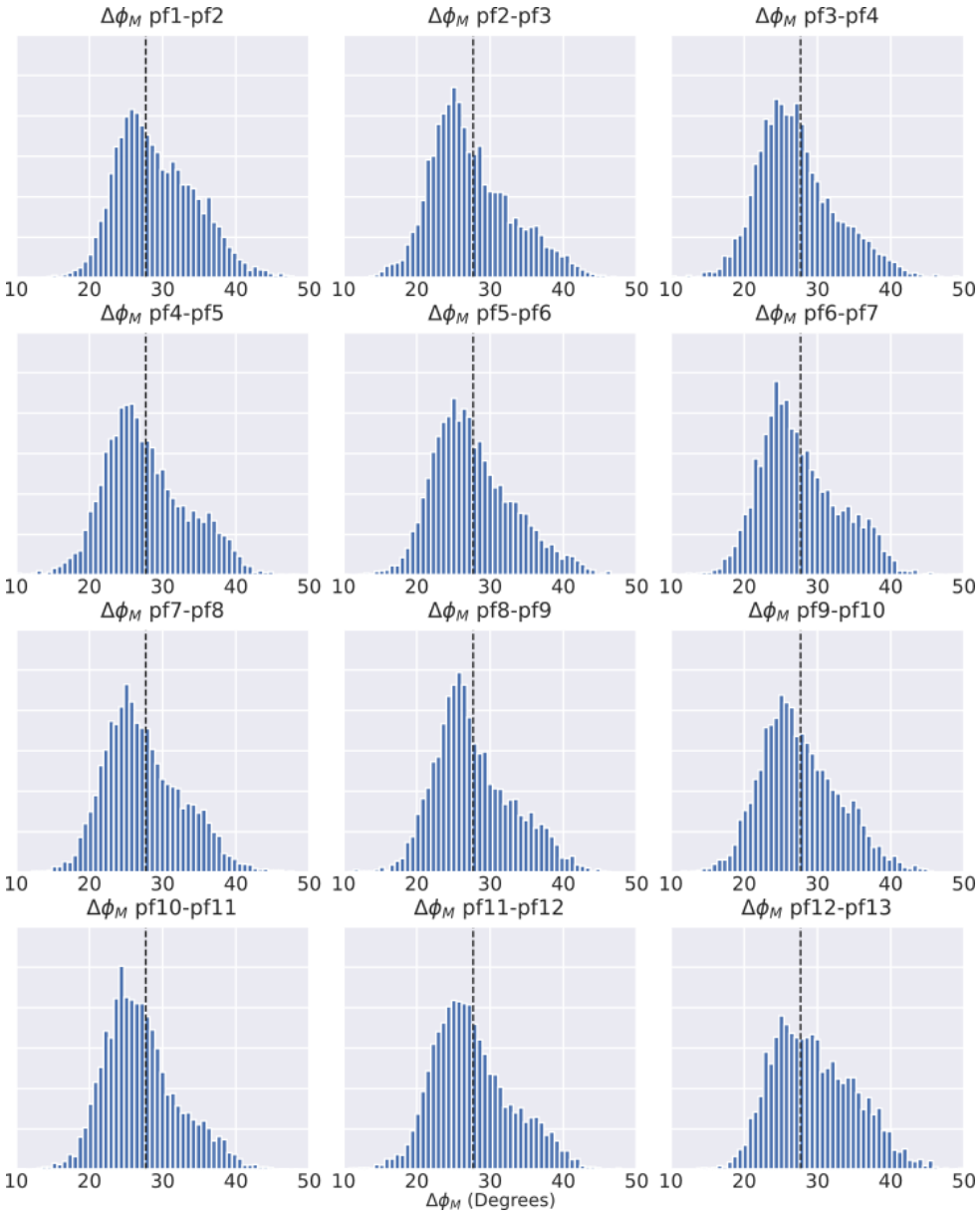

Figure 9: $\Delta\varphi_M$ plots for individual protofilament pairs corresponding to the leftmost peak in the 13PF GMPCPP seam plot. The dashed line represents $\Delta\varphi_E$. While the distribution of the low and high wall curvature state changes for different protofilament pairs, there is always a significant population of the high curvature state for each protofilament pair. Note that the seam distribution plot is not shown.

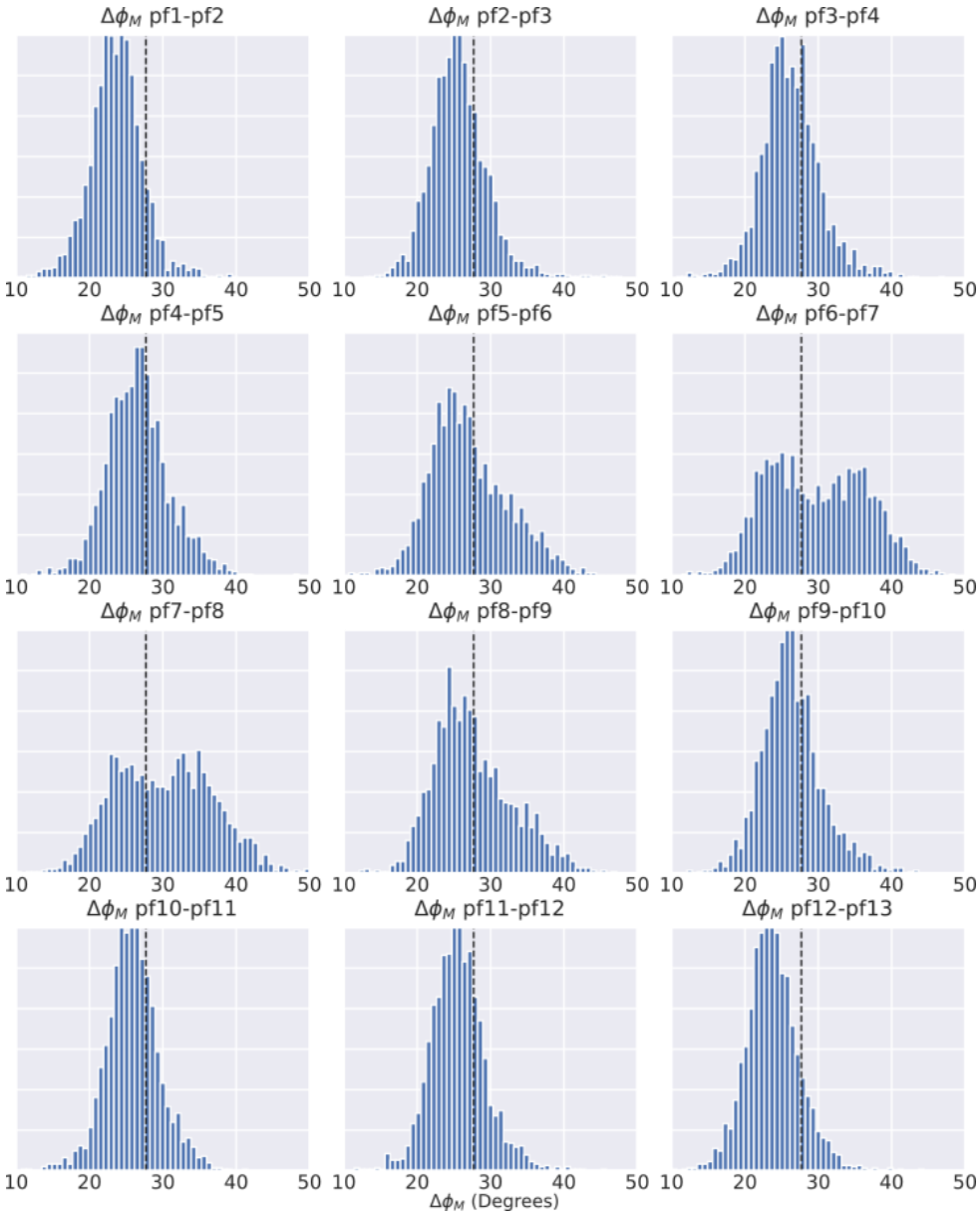

Figure 10: $\Delta\varphi_M$ plots for individual protofilament pairs corresponding to the rightmost peak in the 13PF GMPCPP seam plot. The dashed line represents $\Delta\varphi_E$. The majority of the protofilament pairs prefer the low curvature wall state, although opposite the seam there tends to be a more even distribution of low and high curvature wall states. Note that the seam distribution plot is not shown.

The microtubule wall is flexible

Analysis of the alignment parameters derived from protofilament refinement reveals that the microtubule wall distorts irregularly. Distortions were quantified by using the refined rotation angles of adjacent protofilaments (φ_i and φ_{i+1}) to calculate the angle between these protofilaments ($\Delta\varphi_M$). Comparing this value to a symmetric protofilament geometry ($\Delta\varphi_E = 360/N$, where N is the number of protofilaments) reveals the deviation from helical symmetry (Figure 7A). $\Delta\varphi_M$ was calculated for each adjacent protofilament pair in a microtubule cross section, for every segment of an individual microtubule, and for every microtubule in the dataset. Analysis of $\Delta\varphi_M$ values at laterally adjacent sites reveals a 'crinkling' behavior, demonstrated by sharp and frequent transitions of $\Delta\varphi_M$ above and below the symmetric $\Delta\varphi_E$ value (Figure 7B). This behavior contrasts with previous results indicating that microtubules 'squash' to form cross sections similar to an ellipse (Lacey et al., 2019). For a squashed microtubule, we'd expect $\Delta\varphi_M$ to transition smoothly from above and below $\Delta\varphi_E$. Whether this discrepancy is due to different sample conditions (i.e. different microtubule binding proteins) or the increased sensitivity of our method is not yet known.

The wall curvature for a given microtubule symmetry type spans beyond the range of curvatures expected for 11-15 protofilament microtubules that are typically observed in *in vitro* polymerization reactions. For the 14-protofilament GMPCPP dataset, the observed $\Delta\varphi_M$ values (reflecting the wall curvature) approximately follow a normal distribution (with a minor rightward shoulder) with the majority of the population ranging from 18° to 33°, which correspond to $\Delta\varphi_E$ values for 20 and 11 protofilament microtubules, respectively (Figure 7C). The magnitude of these distortions far exceeds values previously reported in other microtubule structural studies, which do not exceed ~4° (Lacey et al., 2019; Zhang et al., 2015; Zhang et al., 2018). To directly visualize the distorted wall structure, particles corresponding to $\Delta\varphi_M$ angles of 20.7°±1° and 30.7°±1° (5°

above and below the symmetric value) were selectively reconstructed. The measured angles between the reconstructed protofilaments (21.3° and 30.8°) are consistent with the selected $\Delta\varphi_M$ values. Moreover, comparison of the two maps reveals a hinge-like motion between protofilaments, with the axis of rotation centered at the lateral contact site (primarily the m-loop) (Figure 7D).

The microtubule wall exhibits preferred geometries

Analysis of the 13-protofilament sample reveals that the majority of protofilament pairs maintain a similar wall geometry as observed in the 14-protofilament microtubule, as reflected by conserved peak positions in the respective $\Delta\varphi_M$ distributions. However, because the average wall curvature of a 13-protofilament microtubule must increase to account for the loss of a protofilament, part of the microtubule wall must adopt higher curvature. This is accomplished in one of two ways. In the majority of microtubule segments, the seam adopts a 14-protofilament-like wall geometry (left peak, bottom histogram Figure 8A). In this scenario, a minority population of more highly curved wall segments (right shoulder, top histogram Figure 8A) is observed in the non-seam protofilament pairs (Figure 9). Alternatively, in a minority of segments the seam distorts by ~12.5° above the ideal helical symmetry to a wall angle of ~40° (right peak, bottom histogram Figure 8A). In this latter scenario, only a few additional protofilament pairs adopt the more highly curved wall geometry (Figure 10). These data suggest that tubulin in a GMPCPP microtubule prefers to adopt a less curved, 14-protofilament wall geometry, even in 13-protofilament microtubules.

The above results describe a microtubule wall geometry that frequently deviates from helical symmetry (by 5° or more), with especially large deviations (>10°) occurring at the seam. In contrast, previous analyses of 13-protofilament GMPCPP microtubules report a structure with nearly symmetric wall angles for non-seam protofilaments ($\Delta\varphi_M \approx \Delta\varphi_E$) and slightly increased wall

curvature (~3°) at the seam (Zhang et al., 2015; Zhang et al., 2018). While our data produce the same average structure, our analysis indicates this structure represents a conformation that is rarely sampled due to the preference to adopt non-symmetric wall angles. Our results indicate that at the seam, the microtubule wall is most frequently less curved than the symmetric geometry, opposite the behavior of the average structure. Nevertheless, the average curvature at the seam is ~3° greater than the symmetric value (as previously observed) due to the presence of a minority population with a greatly increased wall curvature. These results emphasize that the behavior of the microtubule wall may not be well represented by an average, and that the wall curvature is not necessarily a simple function of protofilament number.

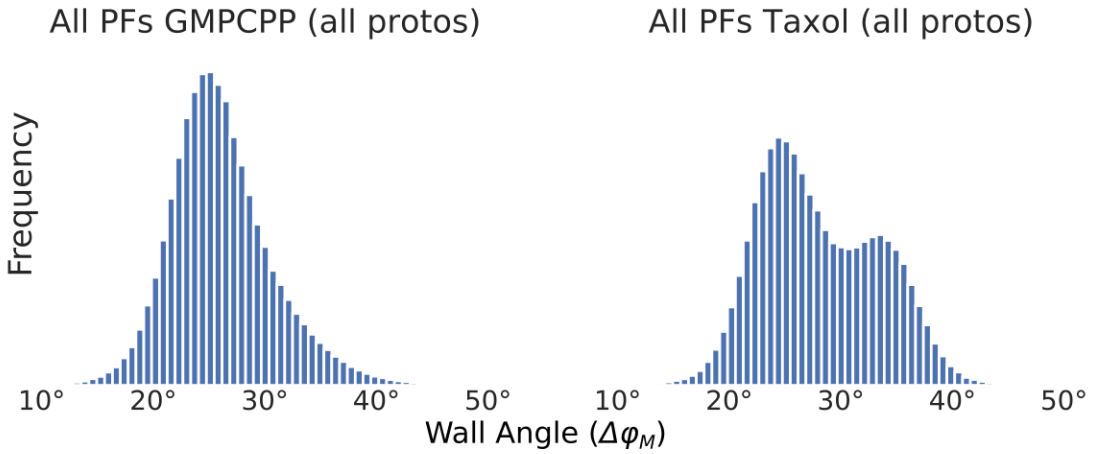

Figure 11: Aggregate $\Delta\varphi_M$ distributions for all microtubules in the GMPCPP and Taxol datasets regardless of the symmetry type. Note the drastic increase in frequency of the high wall curvature state in the Taxol dataset.

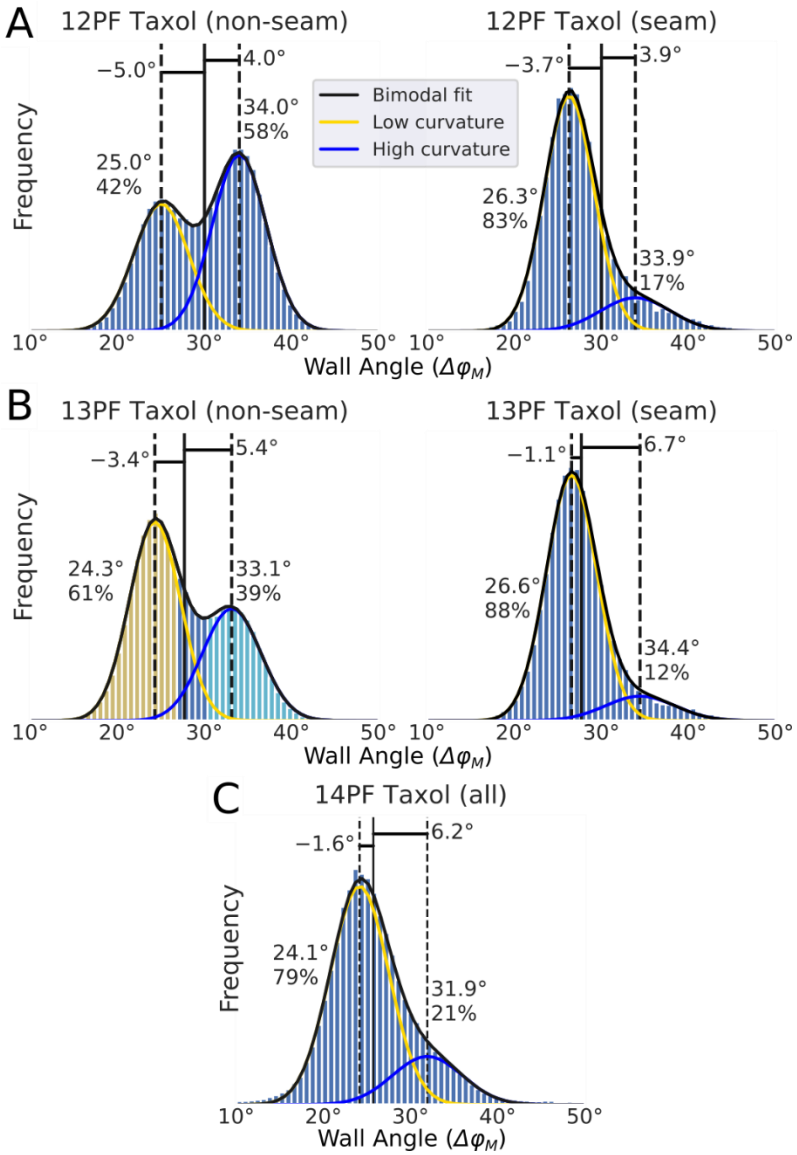

Figure 12: Preferred wall angles are consistent between microtubule symmetry types. (*A, B, C*) Distribution of $\Delta\varphi_M$ for 12, 13, and 14-protofilament microtubules, respectively. All distributions have been fit by a double gaussian curve, with each peak's mean and relative population noted by the respective peaks. The distance of each peak from the symmetric wall angle ($\Delta\varphi_E$, denoted by the solid black line) is also noted above each peak. A shift in distribution from the high angular state to the low angular state can be observed while transitioning from 12 to 13 to 14 protofilament microtubules.

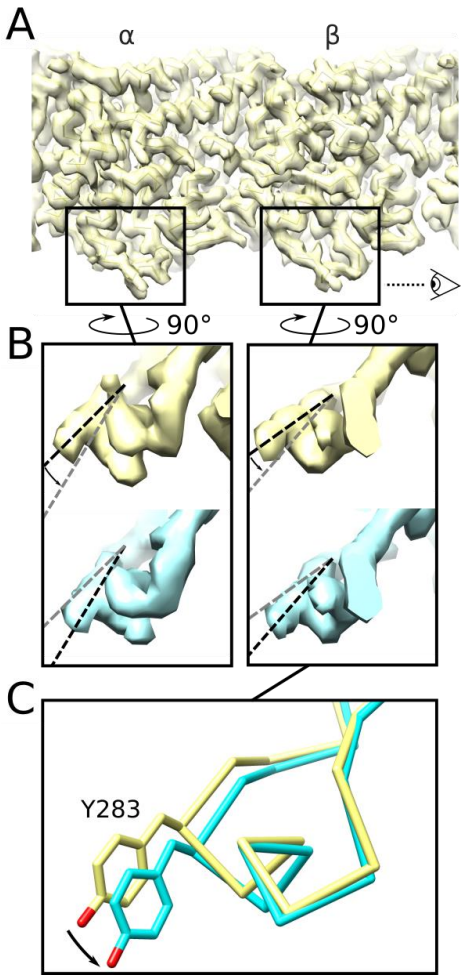

Figure 13: Structural differences between the low and high angular states. (*A*) 3D reconstruction corresponding to particles in the left peak (yellow highlighted region) of the histogram in Figure 12B. (B) Close up of the m-loops in (*A*) (top) and for the equivalent 3D reconstruction of the right peak from the histogram in Figure 12B (bottom). (C) Rotation of the β-tubulin m-loop observed in the refined PDB models from 3D maps in (*B*, right panel).

A shift towards the more curved wall population in Taxol-stabilized microtubules

Similar to the GMPCPP sample, protofilament pairs in the Taxol sample exhibit two populations with distinct wall curvatures, but microtubules tend to adopt symmetry types with higher wall curvature (i.e. a higher percentage of 12 and 13-protofilament microtubules) (Figure 11). In the GMPCPP sample 14-protofilament microtubules were favored over 13 by ~3.6 fold, while this preference was reversed for the Taxol sample; which preferred 13-protofilament microtubules over 14 protofilament ones by ~5.6 fold. Moreover, a substantial population of 12-protofilament microtubules was observed in the Taxol sample, while these were rare in the GMPCPP sample. In spite of these differences, wall angle distributions were quite similar for a given symmetry type between the two sample types. For the Taxol sample, the vast majority of protofilament pairs in 14-protofilament microtubules adopt the low curvature state (Figure 12C), similar to what was observed with the GMPCPP sample (Figure 8B). Also similar to the GMPCPP sample (Figure 8A), the proportion of protofilament pairs in the high curvature state is larger in the 13-protofilament Taxol sample (Figure 12B). Altogether, these data show that the highly curved wall conformation in the Taxol sample is more favored relative to the GMPCPP sample (Figure 11), providing a straightforward explanation for why the average protofilament number is reduced in Taxol microtubules.

While the wall angle behaviors are largely consistent between the Taxol and GMPCPP samples, two differences are evident. First, for the non-seam case, bimodal peaks are more widely separated in Taxol microtubules compared with GMPCPP ones (8.8° vs 8.2° respectively). In addition to being more widely separated, the standard deviation of this second peak is also larger in this GMPCPP case. Together, these data explain why the GMPCPP peaks are less well defined compared with the Taxol distributions. Second, 13-protofilament Taxol microtubules lack the minority, high curvature population observed at the seam in the GMPCPP sample. Both these

differences may be the result of interactions between Taxol and the m-loop (see Discussion as this explanation is more speculative). Furthermore, we note that while there are small differences in peak values between different symmetry and sample types, these differences are likely explained by changes in the local environment (e.g. additional forces due to supertwist).

Two distinct wall geometries are associated with two different tubulin m-loop conformations

High resolution 3D reconstructions of the microtubule wall at low and high curvatures reveals a hinge-like rotation centered at the m-loop. The bimodal wall angle distribution observed in the 13-protofilament, Taxol sample, with clearly separated peaks, provided sufficient numbers of particles to reconstruct protofilament pairs in both low and high curvature states. Curve fitting the non-seam $\Delta\varphi_M$ distribution to a double-gaussian function, provided wall angle estimates for the low and high curvature states (24.3° and 33.1°, respectively (Figure 12B). Reconstructions of particles centered around these values yielded ~3.3 Å structures of both states. Comparison of the two maps reveals that most of the conformational changes associated with the curvature change are localized to the m-loops of adjoining protofilament pairs (Figure 13). Correspondingly, geometric analysis reveals that when one protofilament is held fixed, the second protofilament rotates about an axis runs directly through the m-loop. These observations indicate that the m-loop functions as a flexible hinge, whose local rearrangements translate to large wall geometry shifts corresponding to the low and high curvature states.

Distortion analysis of microtubules of additional symmetry types indicate that the above features are general. Protofilament refinement resolved structures from 12 and 14-protofilament Taxol microtubules to high resolution (3.2 Å and 3.6 Å, respectively). For the 12-protofilament case, the wall angle distribution is bimodal, but with an increased population of the high curvature state (Figure 12A), relative to 13-protofilament case (Figure 12B). Gaussian curve fits also reveal

that the low and high curvature wall geometries for the 12-protofilament microtubules (25.0° and 34.0°, respectively) are consistent with the 13-protofilament case. Moreover, 3D reconstructions of low and high curvature states from the 12-protofilament Taxol sample exhibit hinge-like behavior of the m-loop that is consistent with the 13-protofilament results. For the 14 protofilament case, most protofilament pairs shift to the low curvature geometry, with a minority population in the high curvature state (Figure 12C). Thus, the behavior of the 14-protofilament Taxol microtubules parallels that of the 14-protofilament GMPCPP microtubules. Overall, these data indicate that the m-loop has two favored conformations and changing the relative population of these conformations enables microtubules to accommodate varying number of protofilaments.

Distortions in the microtubule lattice are local

We quantified the 'crinkling' behavior observed in the microtubule wall (Figure 7B) by autocorrelation analysis of neighboring wall angles, which revealed that neighboring wall angles are highly anti-correlated, while correlation is weak for more distant wall angles (Figure 14A). This analysis defines a simple behavior in which deformation of a single protofilament pair has little effect on the remaining protofilaments. In other words, variation of a given wall angle leads to counter-rotation of its corresponding protofilament pair, which is accompanied by smaller changes, of opposite sign, in the two neighboring wall angles, but otherwise leaves the microtubule wall largely unaffected (Figure 15A). This behavior was observed in all symmetry types, across both sample conditions. These data illustrate an irregular microtubule wall geometry that is defined by highly local lateral deformations resulting from preferred m-loop conformations that deviate from perfect symmetry.

In addition to correlation analysis, the average protofilament neighbor response can be measured by selecting a specific microtubule distortion angles (eg: ten degrees below the

expected symmetric value: $\Delta\varphi_D$=-10°). The average $\Delta\varphi_D$ value for the protofilament pairs neighboring the corresponding distortion value is then calculated in order to determine what the average response is (Figure 14C). While this is very similar to calculating the autocorrelation, this method provides a more intuitive result. For instance, given a distortion of $\Delta\varphi_D$=-10° (Figure 14C blue curve), the average response of both nearest neighboring protofilaments is $\Delta\varphi_D$≈5° and the remainder of the protofilaments have an average distortion of 0°. Thus, the same local response observed in the autocorrelation analysis is seen (i.e. strong negative correlation of the nearest neighbors).

Further, we can divide all $\Delta\varphi_D$ values by the original, selected distortion (in this case -10°) in order to see the normalized response and compare the results with other starting distortions values (Figure 14D). Interestingly, there tends to be a difference in neighbor response depending on the magnitude of the initial distortion. For larger distortions, there is a stronger anticorrelated response relative to smaller distortions. This appears true for both positive and negative correlations.

In contrast to the highly local lateral behavior, microtubule wall deformations tend to persist longitudinally along protofilaments for many subunits (Figure 14B). Correlation analysis of $\Delta\varphi_M$ along single protofilaments reveals consistently positive correlation that decays monotonically, but remains positive to a separation of at least 30 subunits. This result suggests that the mechanical coupling between neighboring subunits along a protofilament is strong, consistent with the extensive interface between longitudinally neighboring tubulin subunits.

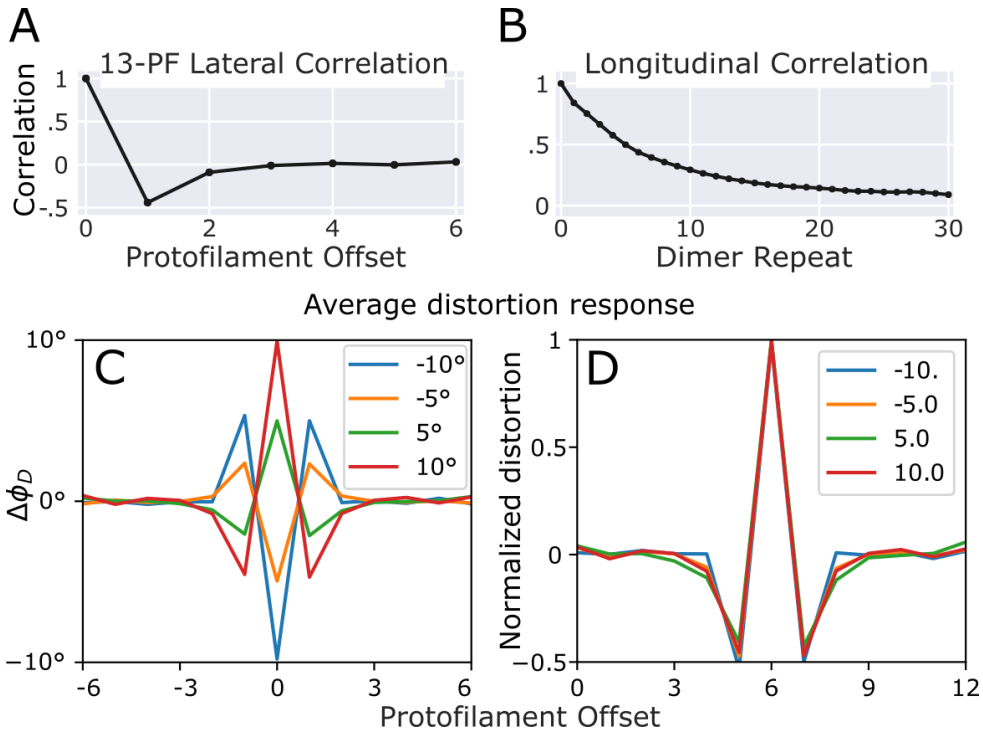

Figure 14: Autocorrelation of wall angles reveals that distortions in microtubules are local. *(A)* Correlation between $\Delta\varphi_M$ values for lateral neighbors in 13 protofilament Taxol microtubules. The plot has been truncated at the point of symmetry, 6 protofilaments away from the initial protofilament. (*B*) Longitudinal autocorrelation plot for 13-protofilament microtubules that are at least 31 subunits long. Note that the length of the protofilament particles used during refinement are ~7 dimers long. (*C*) Average neighboring protofilament response for distortions of varying amplitudes. The initial distortions were selected by finding protofilament pairs with the specified wall angle ($\Delta\varphi_M$) and calculating the average of the remaining protofilament pairs. Left plot shows the actual response, and the right plot shows the 'normalized' response (i.e. neighbors distortion value divided by the initial selected distortion).

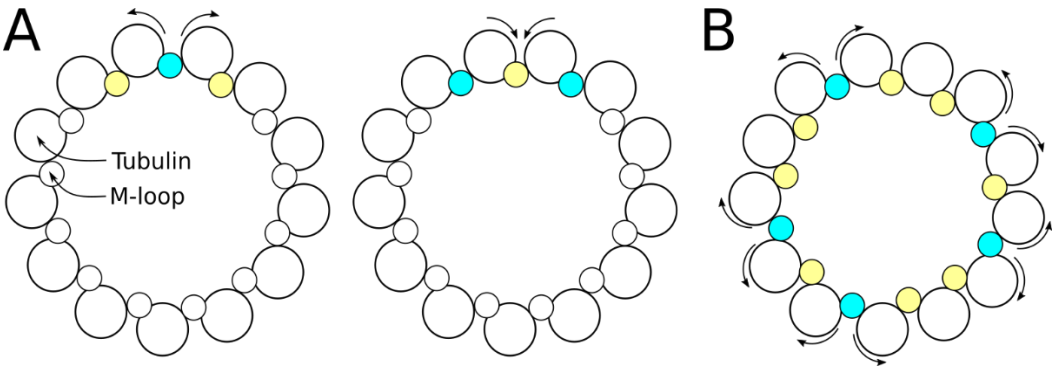

Figure 15: Model of an elemental wall distortion by a protofilament pair. (*A*) Increasing the angle between protofilaments (left), rolls the protofilaments away from each other and simultaneously decreases the angle between the nearest neighbors. Conversely, decreasing the angle between protofilaments (right), rolls the protofilaments towards each other and increases the angle between the nearest neighbors. Thus, distortions of the central angle (cyan/yellow), is opposite the distortion of the two adjacent angles (yellow/cyan), and other wall angles (uncolored) are minimally affected. (*B*) Superposition of many elemental distortions leads to irregular microtubule cross sections as observed in this work.

Discussion

How stabilizing different wall curvature states could change a microtubule's preferred symmetry type

Our results provide a structural rationale for how the inherent behavior of tubulin leads to distributions of microtubules with different symmetry types. Previous work has shown that microtubule symmetry can be influenced by a variety of factors, including stabilizing drugs and protein cofactors (des Georges et al., 2008; Diaz et al., 1998; Kellogg et al., 2017; Moores et al., 2004). Here we have shown that within microtubules, the wall adopts two preferred geometries corresponding to rotation of the m-loop that laterally connects adjacent protofilaments. While neither of these geometries perfectly matches any given microtubule symmetry type, they serve as building blocks that can be mixed and matched to generate microtubules with a variety of different symmetry types. Therefore, stabilizing (or destabilizing) one of these wall geometries provides a mechanism for changing the symmetry type.

Our data indicate that Taxol microtubules may adopt this mechanism because, while the two preferred wall geometries are consistent between Taxol and GMPCPP microtubule samples, the higher curvature state is more populated in the Taxol sample (Figure 11). This result explains why Taxol reduces the number of protofilaments compared with drug free microtubules (Diaz et al., 1998). A probable explanation for this behavior is that direct or indirect interactions between Taxol and the m-loop stabilize the high curvature state. We note that in the high curvature state, the m-loop approaches Van der Waals contact distance with Taxol, indicating a potential role for direct interactions to preferentially stabilize this state. Another role for Taxol may be to restrict larger wall deformations sometimes observed at the seam of the 13-protofilament, GMPCPP sample (Figure 8A). The corresponding ~40° wall angle would move the m-loop even closer to Taxol than the high curvature state (~33° wall angle), likely generating steric overlap. Regardless

of the mechanism, our data indicate that the microtubule seam can make extremely large excursions from helical symmetry, but these are blocked by Taxol.

A striking result of this study is that for 12 and 13 protofilament microtubules, a symmetric wall cross section is disfavored because neither low nor high curvature wall angles are near the wall angle required for symmetry. Therefore, these symmetry types require a mixture of the low and high curvature wall angles with comparable populations of each, leading to irregular wall geometries. In contrast, the low curvature wall angle is significantly more populated in 14-protofilament microtubules, leading to a more uniform wall geometry. Because Taxol microtubules favor the 12 and 13-protofilament forms, these microtubules deviate more from helical symmetry than GMPCPP microtubules, where the 14-protofilament type is more favored. Wall irregularity in the Taxol sample is further amplified due to a larger difference between wall angles of the low and high curvature states compared with the GMPCPP sample. The above observations provide an explanation for why 3D reconstructions of Taxol microtubules exhibit higher anisotropy and lower resolution compared with other sample types (Kellogg et al., 2017).

The microtubule wall behavior observed here is likely to extend beyond the sample conditions examined in the current work. In the absence of drugs or stabilizing protein cofactors, *in vitro* microtubules preferentially adopt the 14-protofilament symmetry type (Moores et al., 2004; Pierson et al., 1978; Zhang et al., 2018), consistent with the wall behavior observed in our GMPCPP sample. In contrast, microtubules *in vivo* almost always adopt the 13-protofilament form (Chaaban and Brouhard, 2017; Tilney et al., 1973), assisted by cofactors that, for example, bind between protofilaments to modify the wall geometry (such as EB3 and doublecortin) (des Georges et al., 2008; Moores et al., 2004; Zhang et al., 2015). Our results indicate that such cofactors could operate by stabilizing the high curvature state. Alternatively, they could operate by shifting the

peak position closer to the wall angle required for symmetry. The methods described in this chapter provide a route to better defining this behavior.

The fact that the microtubule wall so frequently deviates from symmetry demonstrates the limitations of Cryo-EM 3D reconstruction approaches that assume a single fixed geometry of the microtubule wall. While it has long been known that microtubules diverge from symmetry at the seam (Zhang et al., 2015), these results clearly demonstrate that the microtubule wall systematically deviates from helical symmetry, not just at the seam, but throughout its cross-section. As I have shown, averaging of such behavior is not necessarily representative of the underlying structures (Figure 7D, Figure 8C, Figure 13). Microtubule reconstructions strategies that rely on averaging full microtubule segments are thus unable to capture the inherently irregular behavior of the microtubule wall. By characterizing and accounting for this behavior, protofilament refinement and other similar methods are poised to improve our understanding of microtubules and their associated proteins.

Focused classification allows us to investigate heterogeneous microtubules

Focused classification has demonstrated its utility in determining the α/β register of individual protofilaments within the microtubule surface. For the Taxol-microtubules, this proved to be essential as a significant population of microtubules containing multiple seams. Interestingly, only one of the 13-protofilament GMPCPP-microtubules appeared to have additional seams. One explanation for this could be that there is a subset of Taxol-microtubules that were polymerized in the presence of Taxol. Previous research has shown that the critical concentration of tubulin decreases in the presence of Taxol, and microtubules polymerized in the presence of Taxol can have different properties compared to microtubules assembled in the absence Taxol (Schiff et al., 1979; Schiff and Horwitz, 1981). Thus, it would seem possible that the microtubules synthesized in the presence of Taxol could be more likely to contain multiple seams.

Additionally, there is a possibility that GMPCPP is not a perfect GTP analogue, and microtubule synthesized with GMPCPP decrease the likelihood of additional seams. Further analysis will be necessary to make a more definitive conclusion. However, the ability to quantify these additional seams for the first time is a step in the right direction.

Additionally, we have demonstrated the ability to classify proteins bound on the surface of microtubule. While this method has so far only been used to classify kinesin, in theory it should work on other proteins as well. This method will be very useful for studying proteins that might not regularly bind to the surface of microtubules, and thus full decoration and helical reconstruction methods would not be able to resolve a meaningful structure. One example of this could be spastin, a microtubule severing enzyme that, when in the active hexameric state, would be much larger than a single tubulin dimer. Focused classification of the predicted binding site might prove crucial in solving the structure of this protein bound to microtubules for the first time.

Methods

Contribution statement: Methods describing the protein purification, microtubule preparation, Cryo-EM sample preparation, and data collection were adapted from Michael Cha's upcoming publication.

Protein Purification: The same stock of protein was used for the monomeric, human kinesin construct (K349) and dimeric, human Kif5b construct (K420) as used in previous publications from our lab (Liu et al., 2017; Shang et al., 2014).

Microtubule preparation: GMPCPP microtubules were prepared using lab purified tubulin from bovine brain, and polymerized by incubating 5 μM tubulin with 1 mM GMPCPP on ice for 15 minutes, allowing for nucleotide exchange. The solution was then polymerized at 37°C for 3 hours before pelleting the microtubules at 40K RPM (Beckman TLA 120.2 rotor) for 20 minutes. The pellet was then resuspended in EM buffer to a final concentration of ~10 μM. The EM resuspension buffer contained 25 mM Pipes at pH 6.8, 25 mM NaCl, 1 mM EGTA, 2 mM $MgCl_2$.

Taxol-stabilized microtubules were polymerized by resuspending 250 μg of lyophilized bovine tubulin (Cytoskeleton, Denver, CO) into 25 μl of EM buffer with 2 mM GTP added. An initial pelleting step (100K RPM using a Beckman TLA 120.2 rotor, 4°C, 10 minutes) was used removed aggregated tubulin. Next, the sample was incubated for 10 minutes at 37°C before adding an equimolar concentration of Taxol. The sample was incubated for an additional 45 minutes before the microtubules were pelleted through a glycerol cushion (EM buffer with 60% glycerol). The pelleted microtubules were resuspended in EM buffer containing 20 μM Taxol to a final concentration of ~10 μM.

Cryo-EM Sample Preparation: For the GMPCPP microtubule sample with monomeric kinesin, microtubules were mixed with a 2x molar excess of kinesin and incubated for 10 minutes at 24°C. 0.07 units of apyrase (Sigma, St. Louis, MO) was added and incubated for 5 minutes to hydrolyze

any residual ATP. The microtubule-kinesin complex was then pelleted at 14K RPM in a tabletop centrifuge for 15 minutes at room temperature. The sample was resuspended in EM buffer to a final concentration of 4 µM microtubules. 4 µl of sample was then added to a holey carbon grid (Quantifoil, Jena, Germany) without glow discharge. The sample was incubated on the grid for one minute before manual blotting and plunging into liquid ethane.

For the Taxol microtubule sample with sparsely decorated dimeric kinesin, microtubules were mixed with the kinesin at a 27.5% molar ratio with 2 mM ATP. The sample was incubated at room temperature for 10 minutes before the complex was pelleted at 14K RPM in a tabletop centrifuge for 15 minutes. The pellet was then resuspended in EM buffer with 0.2 µM ADP and 0.05% Nonidet P-40 (Sigma-Aldrich, Darmstadt, Germany). This sample was diluted to a final concentration of 0.275 µM microtubules and 4 µl was added to C-flat holey carbon grids (EMS, Hatfield, PA). Grids had been pre-treated using a plasma cleaner (1 second of H_2O_2). After a 1-minute incubation on the grid, the sample was blotted using a Vitrobot with a 2 second blot time and a -2 mm offset before being plunge frozen.

Data Collection: Cryo-EM micrographs were collected on a Titan Krios (FEI, Hillsboro, OR) with K2 direct electron detectors (Gatan, Pleasanton, CA), using SerialEM for semi-automated data collection. For the GMPCPP sample, the total electron dose collected was 65 $e^-/Å^2$ distributed over 40 frames. The dataset (1,527 total micrographs) was collected at 29,000x magnification with an effective pixel size of 0.65Å using super-resolution mode. The defocus was varied between -1 and -2.5 µm. For the Taxol dataset, the total electron dose was 66 $e^-/Å^2$ distributed over 40 frames. However, only the first 15 frames were used for processing. The 5,226 micrographs collected had an effective pixel size of .667Å in super-resolution mode, and the defocus varied from -1.5 to -2.5 µm.

Initial Data Processing: Following data collection, the movies from both datasets were aligned using MotionCor2 (Zheng et al., 2017) and 1x1 grid for motion correction. Magnification distortion correction and dose filtering were both performed during movie alignment. Micrographs from both datasets were also binned by two so that their effective pixel size was near 1.3 Å. CTF estimation was performed with Gctf (Zhang, 2016) using equiphase averaging. Microtubules were then boxed using EMAN's (Ludtke et al., 1999) boxer and each microtubule was segmented into overlapping boxes spaced by ~80 Å.

Traditional Helical Analysis: Following boxing, microtubules were then sorted into different symmetry types. For the GMPCPP-stabilized dataset, the microtubule symmetry was determined as previously described (Sindelar and Downing, 2007). Briefly, each microtubule segment is compared to images generated by projecting a 13 or 14-protofilament microtubule reference volume at various Euler angles. The reference projections with the highest correlation to all microtubule segments determines the microtubule symmetry type as well as the low-resolution Euler angles. In addition to determining the microtubule symmetry type, this method also determines the location of the microtubule seam for the GMPCPP-stabilized dataset due to the complete decoration of the kinesin motor domain. For the Taxol-stabilized dataset, microtubule symmetry was determined using RELION (Scheres, 2012) 3D Classification. Bare 12, 13, and 14-protofilament microtubules were used as reference volumes. One iteration of 3D classification was performed using 0.9-degree angular searches. Microtubules were determined to be of a specific symmetry type if at least 80% of the segments of the microtubule were classified the same. If so, the coordinates were smoothed as previously described (Liu et al., 2017). Note the seam was not found in this case. However, to better compare the helically refined and protofilament refined maps, single seam microtubules were identified (described below) and

high-resolution refinement was also performed exclusively on particles after accounting for the seam location.

Following symmetry sorting high resolution refinement of the microtubules was performed using Helical Refinement in RELION. During refinement microtubules were treated as asymmetric tubes with a helical rise of 82 Å and a helical twist of 0°. Helical parameter searching was turned on in order to find the dimer repeat distance as well as the supertwist during refinement. After this asymmetric helical refinement step, the coordinates can be symmetrized and a final helical volume was generated using the 'good' protofilament as previously described (Sindelar and Downing, 2007; Zhang and Nogales, 2015). Postprocessing and the final resolution of this map was calculated using RELION. Local resolution was calculated using Bsoft (Heymann, 2018).

Protofilament Refinement: For clarity this section will be described for a 13-protofilament microtubule, even though it has been applied to each of the symmetry types in this chapter. After helical analysis, the refined, asymmetric microtubule coordinates were smoothed in preparation for particle subtraction. The final asymmetric volume from RELION was used to generate subtraction volumes by using a wedge masks to remove each unique protofilament in the microtubule volume. This method resulted in 13 different volumes that would be used for subtraction. By using RELION to subtract each volume from a single microtubule segment using the smoothed, asymmetric, microtubule coordinates obtained during helical refinement, a stack of protofilament particles 13 times the original particle stack size was generated. Each protofilament particle was approximately 7 tubulin dimers in length. The smoothed coordinates were then symmetrized so that each protofilament particle aligned to a common reference. These coordinates were then reconstructed to generate a protofilament map that would be used as the starting reference model for protofilament refinement. Additionally, this protofilament map was

lowpass filtered to 20 Å and made into a mask that would be used for refinement. The symmetrized coordinates were then treated as single particles and locally refined in RELION. For the GMPCPP dataset, the data processing ends here.

Protofilament Subtraction: Following protofilament refinement, a second round of subtraction was performed in order to minimize background signal that resulted from an initial, imperfect subtraction. Each microtubule segment was subjected to 12 rounds of subtraction using the protofilament refined coordinates and volume, which allowed for a better subtraction because microtubule distortions could be accounted for. Note, if protofilament subtraction was not performed, subsequent classification steps produced 'worse' results (i.e. weaker kinesin densities or fewer protofilaments registers correctly determined).

Protofilament Register Determination: After protofilament subtraction, tubulin PDB (taken from 3J8X) (Shang et al., 2014) were fit along the length the protofilament and a synthetic volume was generated using these fit PDBs and EMAN's (Ludtke et al., 1999) pdb2mrc command. This volume was used as the α/β register reference volume. The PDBs were then shifted by 40 Å and a second synthetic volume was generated for the β/α register reference volume. These volumes were filtered to 6 Å and used as references for RELION 3D Classification. After classification, a protofilament was determined to be in the α/β or β/α register if 70% of the protofilament particles classified in that register. Additionally, if not all protofilaments in the microtubule were classifiable (i.e. one protofilament had 60% classified as β/α and 40% classified as α/β) the entire microtubule was thrown out of the dataset. All β/α protofilaments were shifted by 40 Å in order to put them in the α/β register. An additional round of protofilament refinement was then run. All PDB fitting was done in Chimera (Pettersen et al., 2004). Following protofilament register determination, a final round of protofilament refinement was performed. The local resolution was

calculated using Bsoft (Heymann, 2018). The same protofilament mask that was used in protofilament refinement was used during classification.

Kinesin Classification: A tubulin kinesin complex PDB (3J8X) (Shang et al., 2014) was fit into the final protofilament volume and a synthetic kinesin only map was generated based off this fit using EMAN (Ludtke et al., 1999). A 50 Å kinesin mask was then generated and the inverse of that mask was then applied to the final protofilament volume in order to generate a protofilament volume with a 'kinesin bite' corresponding to the kinesin binding site (similar to methods described in (Mentes et al., 2018)). This protofilament volume was subtracted from the protofilament particles leaving behind only the kinesin binding site. A 25K particle subset of the data was subjected to 3D classification in RELION. The resulting two classes were then used as reference to seed 3D classification of the full dataset.

PDB Refinement: To visualize an atomic model of the m-loop in the low and high rotational states, COOT was used to relax amino acids in the m-loop, in this case residues 274-287. Because the only region of interest was the m-loop during these refinements, no further structural analysis or validation was done.

Synthetic Microtubule Processing: Two sets of synthetic micrographs were generated as previously described (Liu et al., 2017) with a couple modifications. First, PDBs corresponding to a tubulin-kinesin monomer complex (3J8X) were used to generate the synthetic images. Second, for one of the sets of synthetic micrographs, the parametric model used to define the location of the tubulin-kinesin complex in the microtubule cross-section was perturbed in order to mimic a distorted microtubule. Both sets of microtubule images had the exact same alignment parameters and defocus values, the only difference between them was one set had distortion applied.

Because the images were synthetically generated the 'perfect' alignment coordinates to a microtubule reference were known. These coordinates were used as a starting point for

refinement in order to avoid seam finding. Helical refinement proceeded as described above. For the distorted set of microtubule images image processing continued with protofilament refinement as described above.

Distortion Analysis: Distortion was measured using the determined φ angles for each protofilament and measuring the angle between adjacent protofilaments (i.e. $\Delta\varphi_M = \varphi_n - \varphi_{n+1}$ where n is defined as the protofilament number in the microtubule cross-section). $\Delta\varphi_M$ was calculated for each protofilament in a microtubule segment and every segment in the microtubule. This calculation was performed for every microtubule in the dataset. For reconstructions of specific $\Delta\varphi_M$ ranges, protofilament refined coordinates corresponding to protofilament n were used to reconstruct the un-subtracted microtubule segment particles. PDBs could be fit into protofilaments n and $n+1$ in the resulting microtubule maps and the angle between them were measured in Chimera (Pettersen et al., 2004).

Peak Separation: For data demonstrating bimodal $\Delta\varphi_M$ behavior, a double gaussian curve was fit using Python. For curve fitting, seam and non-seam $\Delta\varphi_M$ data were separated. For the 13-protofilament, GMPCPP seam data, the data was fit as is. For all other data, a bootstrap-like approach was used. The $\Delta\varphi_M$ values were resampled 1000 times and the average mean and standard deviation were used to fit the data. Following peak fitting, data for peak 1 was taken from particles two standard deviations below the mean of peak 2. Data for peak 2 were taken from all particles two standard deviations above peak 1. For the Taxol-stabilized dataset, separated peak data corresponding to both protofilaments n and $n+1$ were subjected to an additional round of protofilament refinement.

Autocorrelation Analysis: Autocorrelation of $\Delta\varphi_M$ was performed in Python. Autocorrelation around a microtubule cross-section was calculated using the following expressions:

$$\Delta\varphi_E = \frac{360}{N}$$

$$\Delta\varphi_D^{i,t}(n) = \Delta\varphi_M^{i,t}(n) - \Delta\varphi_E$$

$$R(a) = \frac{\sum_{t=1}^{T}\sum_{i=1}^{I_t}\sum_{n=0}^{N}\Delta\varphi_D^{i,t}(n)\Delta\varphi_D^{i,t}(n-a)}{\sum_{t=1}^{T}\sum_{i=1}^{I_t}\sum_{n=0}^{N}\Delta\varphi_D^{i,t}(n)^2}$$

Here *N* is the number of protofilaments in the microtubule and *n* is the protofilament offset. Autocorrelation values were calculated for each microtubule (*t*) in the sample (*T;* total number of microtubules), over every axial repeat (*i; I_t* total number of repeats per microtubule *t*). Here, $\Delta\varphi_D^{i,t}$ is subject to a wraparound condition, where $\Delta\varphi_D^{i,t}(-x) = \Delta\varphi_D^{i,t}(N-x)$. Due to the symmetric nature of this result, only N/2 protofilament offsets are displayed.

Autocorrelation along the length of each protofilament was calculated as:

$$R(a) = \frac{\sum_{t=1}^{T}\sum_{n=0}^{N}\sum_{i=a}^{I_t}\Delta\varphi_D^{n,t}(i)\Delta\varphi_D^{n,t}(i-a)}{\sum_{t=1}^{T}\sum_{n=0}^{N}\sum_{i=a}^{I_t}\Delta\varphi_D^{n,t}(i)^2}$$

Here, the right-most sum is restricted within the range $i = a$ to $i = I_t$ due to the lack of wraparound symmetry when $\Delta\varphi_D^{n,t}$ is considered as a function of longitudinal position along a protofilament. For this calculation, microtubules with a minimum length of 34 segments (I_t=34) were selected.

Chapter II: Alternative cryo-EM methods to study the structure of microtubule-bound spastin.

Introduction

Regulation of microtubule dynamics is essential for many different cellular activities and the loss of this regulation can lead to different diseases, including Parkinson's disease and Hereditary Spastic Paraplegia (HSP) (Bailey et al., 2016; Pellegrini et al., 2017). The significance of microtubule dynamic regulation is further emphasized by the fact that approximately one third of all chemotherapeutic drugs affect microtubule dynamics in some way (Borisy et al., 2016). One important microtubule dynamic regulator is the ATPase Associated with diverse cellular Activity (AAA+), spastin. Spastin was initially discovered as the most commonly mutated gene in HSP (Hazan et al., 1999). This disease is primarily characterized by the progressive weakening and loss of function in the lower extremities resulting from degeneration of the corticospinal tract (Errico et al., 2002). Colocalization, genetic, transfection, and biochemical experiments showed that spastin is highly expressed in neurons and functions as a microtubule severing enzyme (Errico et al., 2002; Errico et al., 2004; Evans et al., 2005; McDermott et al., 2003; Molon et al., 2004; Roll-Mecak and Vale, 2005; Sherwood et al., 2004; Trotta et al., 2004). Furthermore, it has been shown that spastin interacts with proteins associated with the centromere and the ESCRT-III complex (Ciccarelli et al., 2003; Errico et al., 2004; Evans et al., 2006; Reid et al., 2005; Svenson et al., 2005). More recently it has been shown that spastin plays an essential role in cell division (Connell et al., 2009). Finally, a recent study has shown that in addition to severing microtubules, spastin also has an ATP-independent activity of decreasing the microtubule shrinking rate and increasing rescue frequency (Kuo et al., 2019). In this way, it can be concluded that by regulating microtubule dynamics in several different ways, spastin plays an important role in a diverse set of cellular processes.

Spastin was shown to be a microtubule enzyme in 2005 (Evans et al., 2005; Roll-Mecak and Vale, 2005), and shortly afterwards a model of severing was proposed based on biochemical

and crystallographic studies. In this model spastin forms a hexameric ring on microtubules and pulls on the C-terminal tail of tubulin. This pulling leads to destabilization of the microtubule lattice and thus results in severing (Roll-Mecak and Vale, 2008). This model is consistent with the requirement of the tubulin tail for binding and severing activity and the fact that excess tubulin tail peptides leads to severing inhibition (Eckert et al., 2012; Roll-Mecak and Vale, 2008; White et al., 2007). Additionally, recent studies showed the effect of tubulin tail modifications on severing activity (Valenstein and Roll-Mecak, 2016). However, until more recently, structural insights into the mechanism of spastin has been lacking.

A big structural breakthrough in severing activity started in 2017, when the structure of katanin, a closely related microtubule severing enzyme, was solved using cryo-EM (Zehr et al., 2017). Two distinct states of katanin had been solved. The first structure demonstrated a hexameric ring that doesn't fully close and instead more closely resembles a 'split lock-washer'. The second structure displayed a closed ring conformation, although this structure is still asymmetric, with the first and last subunits of the hexamer skewed at the point of contact. These structures gave rise to the hypothesis that by ratcheting between these two conformations in an ATP hydrolysis dependent manner, the tubulin tail could be fed through the pore of the hexamer, leading to severing activity. More recently, a 3.2 Å structure of hexameric spastin bound to a polyglutamate peptide was solved (Sandate et al., 2019). This structure closely resembled the split lock-washer conformation observed in the katanin structure. However, no closed ring structure was found. While these structures have certainly been a breakthrough in the severing field, more work is still necessary.

One of the more interesting areas of future structural studies with spastin lies with solving the structure of spastin (or other microtubule severing enzymes) bound to microtubules. However, because spastin binds to microtubules in an irregular manner, this poses a problem for

cryo-EM reconstruction techniques, that rely on helical symmetry to refine the structure. While the previously discussed joint approach of protofilament refinement and focused classification should be able to solve the structure of most microtubule associated protein, sufficiently large structures, such as spastin, could potentially also be resolved using alternative approaches. In this chapter I will discuss the layer line masking method and the benefits and shortcomings of this approach when studying an enzyme like spastin, or other large microtubule binding proteins.

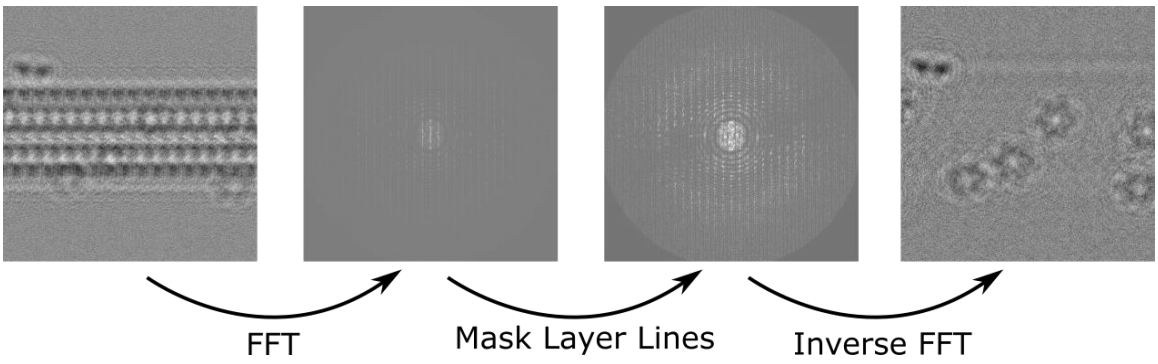

Figure 16: Layer line masking workflow. Following microtubule particle selection and extraction, the FFT of boxed microtubule segments is taken. The column of the FFT containing the layer lines are then set to zero and the inverse FFT is taken. This result is the boxed segment with the microtubule subtracted; any bound protein density remains.

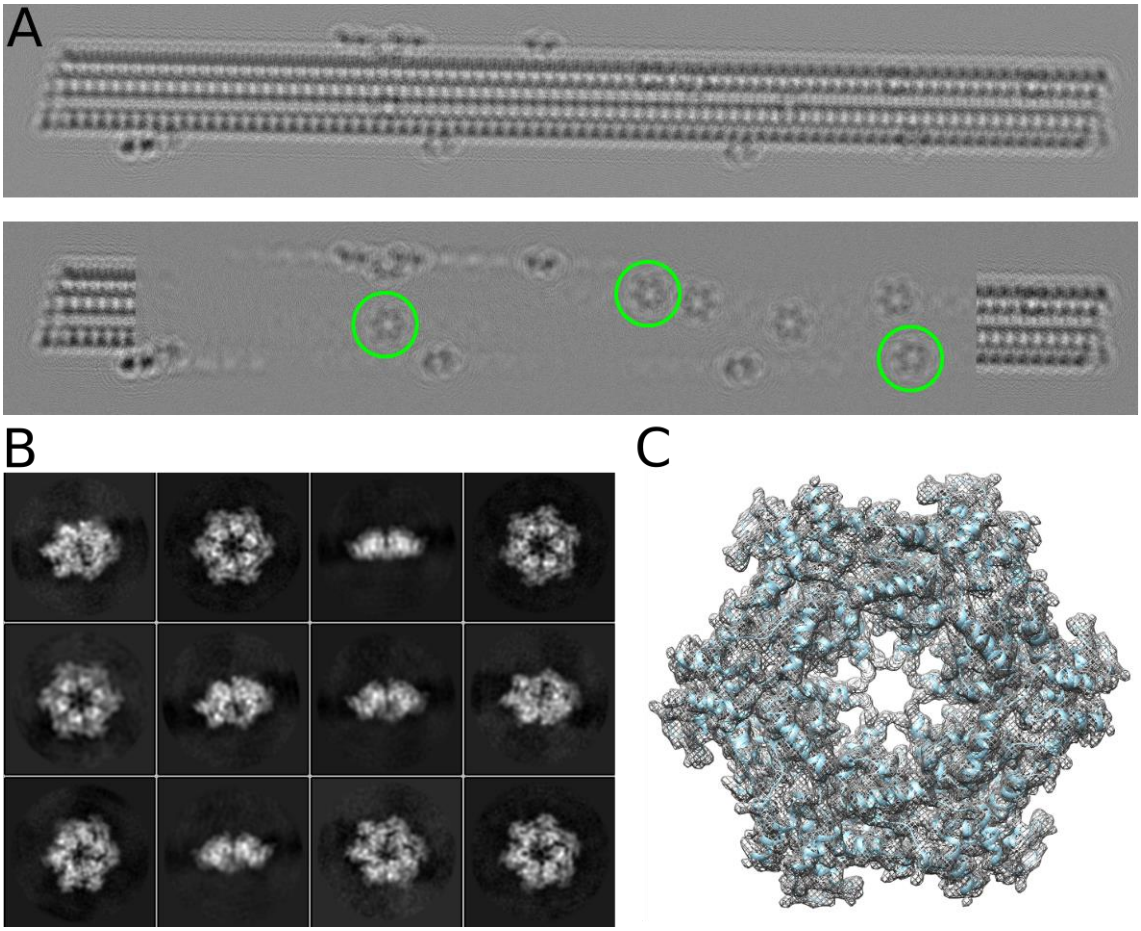

Figure 17: Processing results from layer line masking. *(A)* Synthetic microtubule with sparsely decorated spastin (top). The same synthetic microtubule, following layer line masking (bottom). Particles can then be selected from this image. Spastin particles circled in green are used to illustrate how picking particles following masking can become much easier. *(B)* 2D classification results of selected spastin particles for a sample, synthetic dataset. *(C)* 3D Refinement result of the same synthetic, spastin particles that were classified in *(B)*.

Results

Layer line masking subtracts microtubules prior to refinement

By setting all points within layer lines to zero, microtubules can be subtracted from an image. Using the radon transform method (Li et al. 2002), the in-plane rotation and helical repeat spacing for a microtubule segment can be found. Using this information, the microtubule particle can be rotated and scaled such that each layer line is vertical, and the width of each layer line is approximately one pixel. This means that by simply setting each column in Fourier space that contains a layer line to zero, the microtubule can effectively be erased (Figure 16). Note that because each microtubule particle is not infinite, aliasing artifacts will occur near the edges of the particle boxes. However, the majority of the remaining density within these boxes will belong to the particle of interest, in this case, spastin.

While layer-line subtraction works on a per microtubule segment basis, the particles of interest becomes convoluted within multiple overlapping microtubule particles. This means actually picking your particles becomes a challenge because there are several copies of the same spastin particle, in one particle stack. This problem occurs because the selected microtubule particles are overlapping, a necessary step in microtubule processing. However, rather than trying to carefully select unique spastin particles, a new micrograph can be generated by returning the subtracted particles back to the original micrograph. Because the center of the subtracted particles contains the fewest aliasing artifacts, the center ~80Å (i.e. the helical repeat distance and thus particle spacing) are returned to the micrograph. This is done for each extracted particle in the stack, resulting in the original micrograph, except with a subtracted microtubule (Figure 17A). Spastin particles can then be selected from these micrographs. Interestingly, spastin particles that could not be seen prior to microtubule subtraction become easy to distinguish.

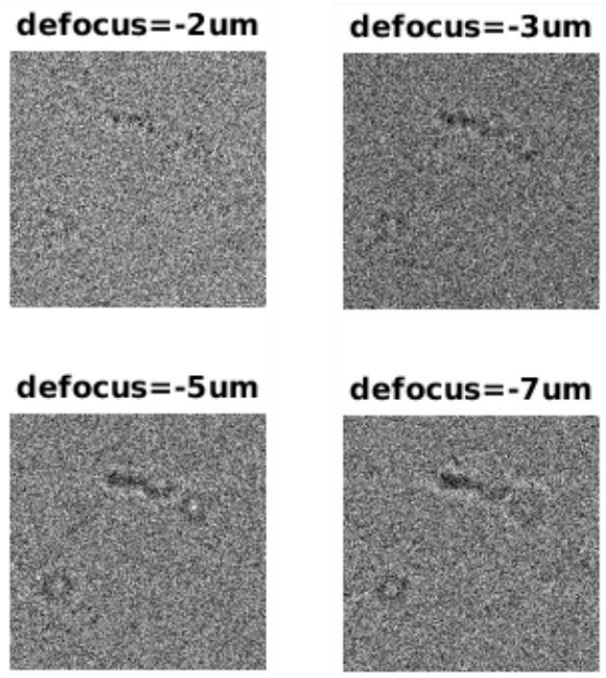

Figure 18: Higher defocus images display clearer spastin density for synthetic images with low signal to noise.

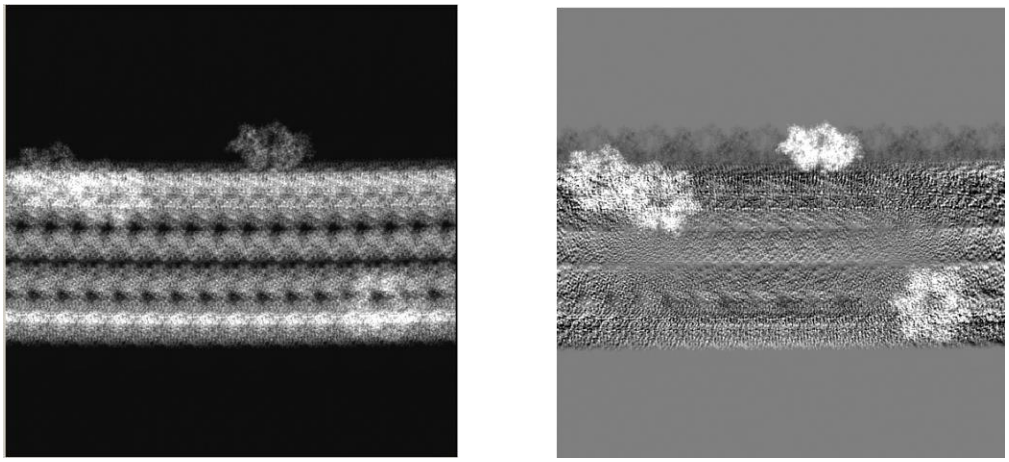

Figure 19: Poor subtraction of microtubule density following layer line masking due to longitudinal curvature.

Reconstruction of particles from layer-line masked regions

Reconstruction of synthetic spastin particles following layer line masking results in a high-resolution structure. To ensure that removing a portion (~20%) of Fourier space wouldn't affect alignment of the remaining particles, a dataset of synthetic micrographs containing spastin microtubules were generated. Microtubule particles were extracted, subjected to layer-line subtraction, and returned to the micrograph as subtracted particles as described above. The spastin particles were then selected and refined as single particles using RELION (Scheres, 2012). By using 2,339 particles with C6 symmetry (equivalent of 14,034 particles), the refinement resulted in a 3.2 Å structure of spastin, suggesting that this method is capable of high-resolution refinement of microtubule bound particles (Figure 17C).

Because recent results have shown that the spastin structure is likely not symmetric when bound to microtubules (Sandate et al., 2019), using C6 symmetry with experimental images will not be ideal. An additional 3D refinement of the same 2,339 particles was performed without imposing any symmetry. The result was an ~8 Å structure of spastin suggesting that applying symmetry is not necessary to obtain a meaningful structure. While the overall resolution of this structure is very low, there were very few particles used as the test was just proof of principle.

Limitations of applying layer-line masking to experimental data

For images with low signal to noise (i.e. similar to experimental conditions), using a higher defocus can help with particle selection. To test this, I generated one synthetic microtubule image with a lot of random noise, and then applied a series of CTFs to the micrograph, each with a different defocus value. The resulting micrographs contained the same microtubule, with the same noise, and only differed by the defocus value of the CTF. Layer line masking was then applied, and the resulting particle images were then compared (Figure 18). For images with high noise and a low defocus value, the spastin particles were hard to distinguish. However, images

with a higher defocus value contained spastin particles that were easier to distinguish. This result suggests that collecting experimental data at higher defocus values may be essential for particle picking.

In general, collecting images at higher defocus is less desirable as a lot of the high-resolution features are lost in the corresponding reconstructions. However, our lab has previously made use of “defocus jumps”, wherein micrograph movie data is initially collected at a low defocus, before the final frames of the movie are collected at a high defocus (Liu et al., 2017). This technique allows for the high-resolution information to be retained in the initial frames of the collected movie data, but the particles can be selected using the movie frames from the high defocus portion. Thus, the resulting reconstruction retains the best of both worlds.

Unfortunately, a major limitation of the method, is that layer line masking works very poorly for curved microtubules. Using synthetic data and applying layer line masking to a curved microtubule particle yielded a subtraction with a significant amount of remaining microtubule density (Figure 19). This poor subtraction is likely a result of the layer-lines blurring as they get farther from the center of the FFT, such that the layer lines width will always exceed one pixel. While this problem is likely solved by zeroing out more pixels in the FFT to account for this behavior, removing more of the FFT will also remove data from spastin, the particle of interest. This problem illustrates the necessity to find a balance between removing enough of the layer lines in the FFT to obtain a good enough subtraction, while leaving enough data behind to reconstruct the particle of interest at high resolution. However, this solution has not yet been tested, and moving forward, a more thorough investigation of this problem would be needed.

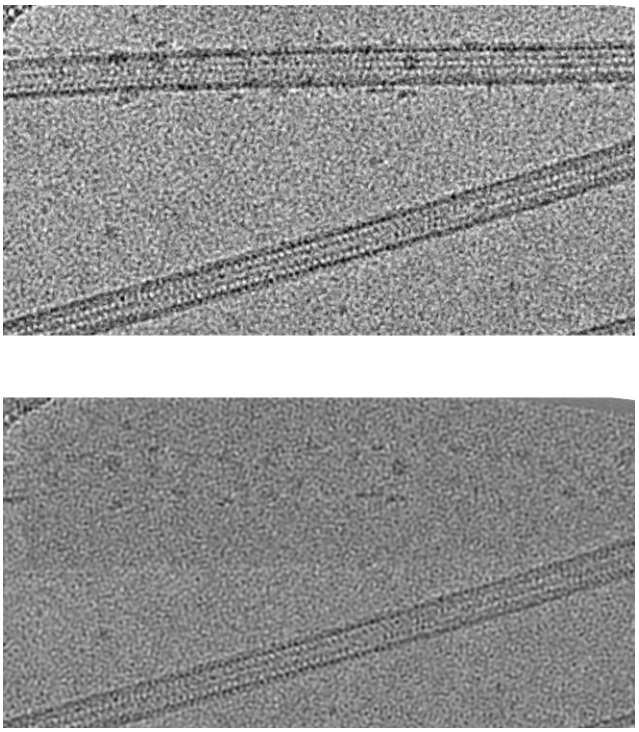

Figure 20: Layer line masking of experimental data yields a micrograph with subtracted microtubule density and visible spastin density.

Layer line masking successfully subtracts microtubules in experimental data

Despite these potential shortcomings, the layer-line masking method was applied to experimental data yielding promising results. Similar to synthetic data, full microtubules could be subtracted from the original micrograph leaving behind the bound spastin particles (Figure 20). Unfortunately, obtaining microtubules with sufficient spastin decoration (and not over decoration) was difficult. Spastin tended to bundle microtubules, and binding appeared to be cooperative. Ultimately this meant that I was unable to obtain an experimental reconstruction of microtubule-bound spastin. However, these preliminary results are promising and suggest that with enough quality data, a reconstruction does seem plausible.

Discussion

In this thesis, I have presented two methods for reconstructing irregularly bound, microtubule associated proteins: layer-line masking and the joint protofilament refinement and focused classification strategy. Each of these methods has their benefits and faults, thus a comparison of the two methods is useful moving forward as each method may have higher utility under different circumstances.

First, a major benefit of the layer-line masking method is that it is very quick compared with protofilament refinement. There is no need for any refinement prior to subtraction, which greatly reduces computational time and allows for a quick quality check of the particles of interest. For example, following microtubule subtraction and particle selection, 2D classification can be used to determine if there is enough high-quality data to move forward with a full 3D refinement. The entirety of this processing can be done relatively quickly.

However, there are limitations of the layer-line masking method as well. First, the particle of interest must be large enough to see during particle selection. This restriction rules out studying particles like kinesin motors, which are smaller than a tubulin dimer. Additionally, there is currently a requirement that all analyzed microtubules must be straight. However, as previously mentioned, further optimization of this method may remove this requirement. Lastly, an additional technicality arises during data collection, wherein a focal jump must be used. The resulting high-defocus micrograph frames can then be used for more accurate particle selection. However, this extra step during data collection is only really a problem if storage space is limited and/or using much older data collection software.

Another major limitation of layer-line masking, is that reconstruction of the spastin particles will not necessarily result in an interpretable microtubule density. Unless spastin is binding to microtubules in a well-defined manner (which seems unlikely), reconstruction of the

spastin particles using the un-subtracted, microtubule images will not yield a volume with a tubulin density of any reasonable quality. However, if spastin binding does have a well-defined interaction interface, then classification of the previously mentioned reconstruction could potentially reveal that interface. Regardless, even if no meaningful tubulin-spastin interface could be discerned using either of these methods, the solved structure of spastin would still be extremely important.

One major benefit of the protofilament refinement and focused classification strategy, is that the tubulin-spastin interface would be well defined. However, if spastin is not binding in a regular manner, then the quality of the spastin reconstruction would be compromised. Additional classes of the bound spastin may reveal distinct binding modes, but this would mean a significantly large number of spastin particles would be needed. Ultimately, I would expect that the resulting spastin resolution would be lower when compared with a volume obtained using layer-line masking.

Another benefit of using protofilament refinement and focused classification, would be the ability to perform distortion analysis on microtubules with bound spastin. This presents an additional layer of analysis that could lead to insights into how spastin is disrupting the microtubule structure as a whole. Additionally, this analysis could be done using particle locations determined using layer line masking. Distortion analysis could reveal if the binding of spastin disrupts the microtubule cross-section, and how far that disruption is propagated down the microtubule length. Furthermore, distortion analysis doesn't even rely on a reconstruction of spastin. This means that if, for whatever reason (i.e. too few particles, too much heterogeneity, etc...), meaningful data can still be elucidated from micrographs containing spastin (assuming an adequate control).

Ultimately, these discussion points bring up that neither method is perfect for analyzing images with spastin, but both can provide unique and valuable information. While layer line masking may seem the most likely to obtain a structure of a heterogenous structure bound on the surface of microtubules in an undefined way, there is no guarantee that the tubulin-spastin interface will be well defined. Additionally, while protofilament refinement and focused classification is not guaranteed to give a high-resolution structure of the bound spastin, distortion analysis can still be used to determine how spastin is affecting the overall microtubule structure. While spastin is the example being used in this discussion, any large microtubule binding protein could benefit from these types of analyses.

Methods

Spastin Purification: The human spastin construct, containing the hydrolysis deficient Walker B mutant (Δ1-227 E442Q) was expressed on a pGEX-6P-3 plasmid. Following transformation in BL21 *E. coli* cells, 4 liters of culture was grown in LB broth (10 g tryptone, 5 g yeast extract, 10 g NaCl per liter) containing 100 μg/ml of Ampicillin and 30 μg/ml of chloramphenicol. Cells were grown at 37° C until reaching an OD_{600} of ~0.8. Cells were then induced with 0.5 mM IPTG and incubated for 5 hours at 30°C. Cells were pelleted at 4K RPM for 10 minutes and either used directly or stored at -80° C.

Cells were then resuspended in 40 ml of lysis buffer per 10 g of cell pellet. Lysis buffer contained 50 mM Tris-HCl, 150 mM NaCl, 5 mM $MgCl_2$, 5 mM DTT, 1 mM ATP, and 1 protease inhibitor tablet, and titrated to a pH of 8. Following resuspension, cells were lysed via sonication for 3 minutes with 1 second on, and 1 second off. Triton was added to 1% concentration and cell debris was pelleted at 40K RPM (Beckman Ti60 rotor) for 30 minutes at 4° C. Lysate was then added to a GSTrap (GE Life Sciences) column using an equilibration buffer, which is the same as lysis buffer, but with 500 mM NaCl and no ATP. Protein was then cleaved on column by adding 160 units of PreScission protease per 1 mL GST column. PreScission protease was diluted in 1 mL of exchange buffer, which contained 50 mM HEPES, 150 mM NaCl, 5 mM $MgCl_2$, and 1 mM DTT, and titrated to a pH of 7.4. The column was then incubated for 5 hours at 4° C to allow for total cleavage. Protein was then eluted using exchange buffer. Protein was either used directly or stored at -80° C following snap freezing in liquid nitrogen.

Thawed protein was subjected to a final round of purification using size exclusion chromatography. Protein was run through a Superdex 200 (GE Life Sciences) size exclusion column using exchange buffer with 1 mM ATP added. The fractions corresponding hexameric spastin were collected as this contained the active protein. Purified spastin was then immediately used.

Cryo-EM Sample Preparation and Data Collection: Taxol stabilized microtubules were prepared as described in the previous chapter. Cryo-EM grids were prepared in a variable manner as an ideal condition was never successfully nailed down. However, the most successful grids tended to add 4 µl of sample to a single grid. This sample would contain between 3-5 µM of MTs, 1-2 µM concentration of spastin, and 1mM ATP. The sample was incubated on the grid for ~1 minute prior to being manual blotted and plunged into liquid ethane. Grids were not glow discharged prior to the sample being added.

Cryo-EM micrographs were collected on a FEI F20 with a K2 direct electron detector (Gatan, Inc.). Data was collected at ~29,000x magnification with an effective pixel size of 1.247Å. The defocus was varied between -1.5 and -5 µm.

Initial Data Processing: After data collection, the movies were aligned using a 1x1 grid in MotionCor2 (Zheng et al., 2017). Dose filtering was performed during movie alignment. CTF estimation was performed with Gctf (Zhang, 2016). Microtubules were then boxed using EMAN's (Ludtke et al., 1999) boxer and each microtubule was segmented into overlapping boxes spaced by ~80 Å.

Generating Synthetic Images: Synthetic images were generated as described in the previous chapter with a few differences. First, rather than using a tubulin-kinesin complex as the model PDB, a tubulin-spastin complex was used. Since no hexameric spastin PDB models existed, I generated one using a similar method as was previously described (Roll-Mecak and Vale, 2008). A PDB of monomeric spastin (3B9P) (Roll-Mecak and Vale, 2008) was replicated 6 times and fit to the subunits in an NSF hexamer (1NSF) (Yu et al., 1998) using Chimera (Pettersen et al., 2004). This hexameric spastin model was then positioned relative to a tubulin PDB (3J8X, tubulin portion only) (Shang et al., 2014) as had previously been suggested (Roll-Mecak and Vale, 2008). Next, rather than using the PDB exclusively to generate synthetic microtubule images, PDBs for the

tubulin-spastin complex and bare tubulin were mixed in a 1:10 ratio so that only 10% of particles in a given microtubule would have spastin bound. This partial decoration was necessary because if there was too high of a spastin density, there would be a lot of overlap in bound particles. Synthetized micrographs had a pixel size of 1.247 pixels/Å and the microtubules had a dimer repeat distance of 81.7 Å, because apparently the idea of simplification was lost on me in the early years of my graduate work.

Layer Line Masking: Once micrographs were synthesized or collected, microtubule particles were boxed using EMAN (Ludtke et al., 1999) as described in the previous chapter. Boxed particles were extracted using EMAN's Python package. The in-plane rotations of these particles are then estimated using the previously described radon transform method (Li et al., 2002). In brief, the microtubule particles are rotated in-plane and a 1D projection of the corresponding power spectrum is collected. If the rotation results in the microtubule axis lying perpendicular to the projection angle, large peaks will occur where the layer lines should be. Finding the in-plane rotation angle with the largest peaks determines the best estimate for this value. Additionally, once the in-plane rotation has been determined, the spacings of the layer-line peaks can help estimate the dimer repeat distance.

After the in-plane rotation angle and dimer repeat distance has been determined, particles are rotated such that the microtubule axis runs from left to right (ie: lies on the x-axis) and the 'ideal' box size is determined. The ideal box size, is the size which will result in the width of a layer line is as close to one as possible. In other words, the number of pixels between each layer lines (henceforth called the spacing) is as close to a whole number as possible. We can calculate the spacing, and thus the box size using the following.

$$spacing = \frac{box\_size * pixel\_size}{dimer\_repeat\_distance}$$

$$box\_size = \frac{spacing * dimer\_repeat\_distance}{pixel\_size}$$

In the case of our synthetic micrographs, the repeat distance is 81.7 Å and the pixel size is 1.247. Thus, a spacing of 7, 8, or 9 pixels would require a box size of 458.6, 524.1, and 589.7 pixels, respectively. Since, 524.1 is closest to a whole number, a box size of 524 is selected (corresponding to a spacing of 7.99, which is reasonably close to 8). Note the value of the spacing is fairly arbitrary, but setting upper and lower limits on the box size can restrict this number. Furthermore, larger spacings are favored as this means less of Fourier space is deleted during layer line masking.

Once the ideal box size and spacing have been determined, particles are re-extracted at the ideal box size. The FFT of each particle is calculated and columns of pixels corresponding to where *x=spacing*n* where n is an integer and its maximum value is when x equals the box size. This process effectively sets all values corresponding to the layer-lines equal to zero. The inverse FFT for the particle is then calculated resulting in an image with a subtracted microtubule segment. The middle ~80 columns of the subtracted particle (corresponding to ~100Å) are returned to the original micrograph and this process is repeated for each repeat in the microtubule.

Spastin refinement: Following layer-line masking, spastin particles were selected from micrographs with the subtracted microtubules. 2D Classification was performed in RELION (Scheres, 2012) and the 'good' classes were selected and used for 3D classification. Again, the particles corresponding to the 'good' class were selected and refined using 3D Refinement in RELION with and without C6 symmetry. This procedure was fortunately very straightforward because synthetic data was used. However, experimental data did not proceed past the 2D classification step as I did not have enough particles for even one 'good' class.

Appendix I: FSC curves

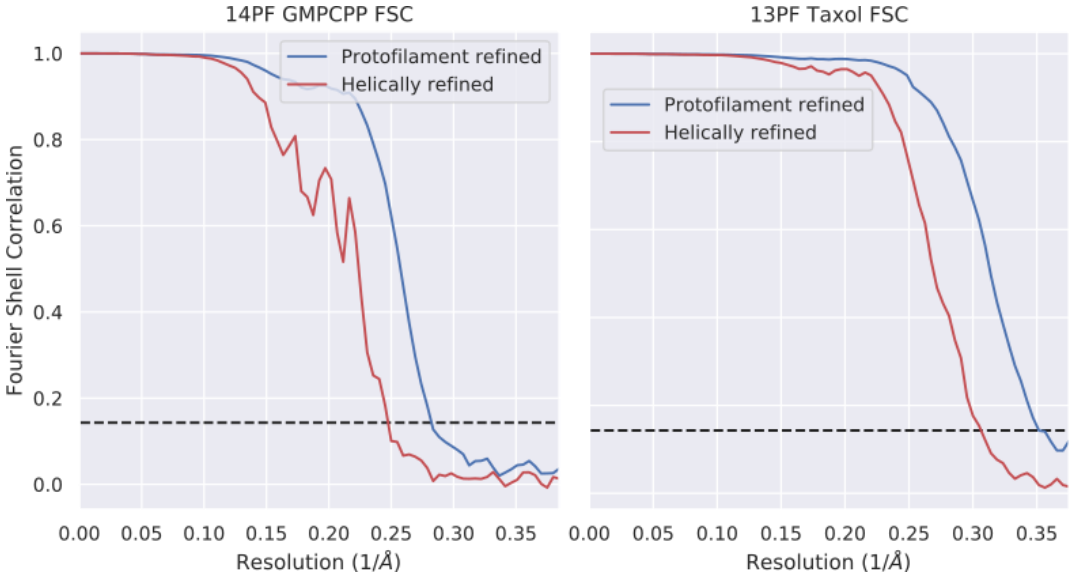

Figure 21: FSC curves for the helically and protofilament refined structures for the 14PF GMPCPP and 13PF Taxol sample.

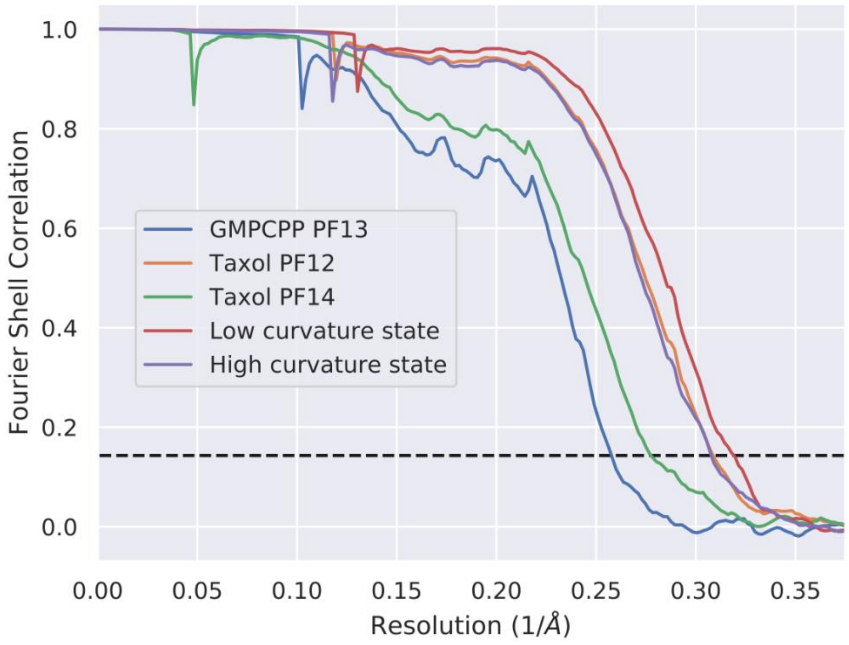

Figure 22: FSC curves of remaining mentioned structure

Appendix II: Spastin Purification

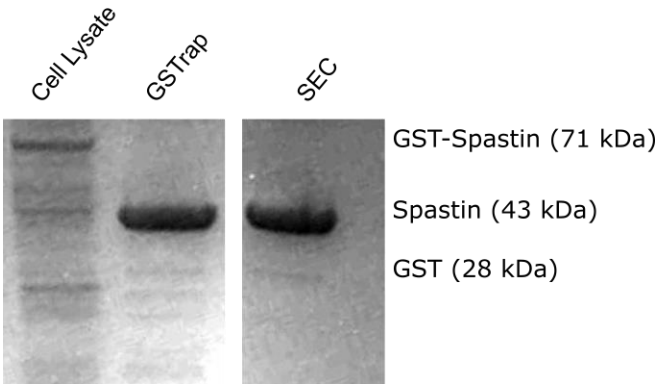

Figure 23: SDS PAGE gel of spastin during the different purification steps.

References

Alushin, G.M., Lander, G.C., Kellogg, E.H., Zhang, R., Baker, D., and Nogales, E. (2014). High-resolution microtubule structures reveal the structural transitions in alphabeta-tubulin upon GTP hydrolysis. Cell *157*, 1117-1129.

Amos, L.A., and Baker, T.S. (1979). The three-dimensional structure of tubulin protofilaments. Nature *279*, 607-612.

Andreu, J.M., Bordas, J., Diaz, J.F., Garcia de Ancos, J., Gil, R., Medrano, F.J., Nogales, E., Pantos, E., and Towns-Andrews, E. (1992). Low resolution structure of microtubules in solution. Synchrotron X-ray scattering and electron microscopy of taxol-induced microtubules assembled from purified tubulin in comparison with glycerol and MAP-induced microtubules. J Mol Biol *226*, 169-184.

Bai, X.C., Rajendra, E., Yang, G., Shi, Y., and Scheres, S.H. (2015). Sampling the conformational space of the catalytic subunit of human gamma-secretase. Elife *4*.

Bailey, M.E., Jiang, N., Dima, R.I., and Ross, J.L. (2016). Invited review: Microtubule severing enzymes couple atpase activity with tubulin GTPase spring loading. Biopolymers *105*, 547-556.

Beese, L., Stubbs, G., and Cohen, C. (1987). Microtubule structure at 18 A resolution. J Mol Biol *194*, 257-264.

Borisy, G., Heald, R., Howard, J., Janke, C., Musacchio, A., and Nogales, E. (2016). Microtubules: 50 years on from the discovery of tubulin. Nat Rev Mol Cell Biol *17*, 322-328.

Borisy, G.G., and Taylor, E.W. (1967a). The mechanism of action of colchicine. Binding of colchincine-3H to cellular protein. J Cell Biol *34*, 525-533.

Borisy, G.G., and Taylor, E.W. (1967b). The mechanism of action of colchicine. Colchicine binding to sea urchin eggs and the mitotic apparatus. J Cell Biol *34*, 535-548.

Brinkley, W. (1997). Microtubules: a brief historical perspective. J Struct Biol *118*, 84-86.

Brouhard, G.J., and Rice, L.M. (2018). Microtubule dynamics: an interplay of biochemistry and mechanics. Nat Rev Mol Cell Biol *19*, 451-463.

Bryan, J., and Wilson, L. (1971). Are cytoplasmic microtubules heteropolymers? Proc Natl Acad Sci U S A *68*, 1762-1766.

Chaaban, S., and Brouhard, G.J. (2017). A microtubule bestiary: structural diversity in tubulin polymers. Mol Biol Cell *28*, 2924-2931.

Ciccarelli, F.D., Proukakis, C., Patel, H., Cross, H., Azam, S., Patton, M.A., Bork, P., and Crosby, A.H. (2003). The identification of a conserved domain in both spartin and spastin, mutated in hereditary spastic paraplegia. Genomics *81*, 437-441.

Conde, C., and Caceres, A. (2009). Microtubule assembly, organization and dynamics in axons and dendrites. Nat Rev Neurosci *10*, 319-332.

Connell, J.W., Lindon, C., Luzio, J.P., and Reid, E. (2009). Spastin couples microtubule severing to membrane traffic in completion of cytokinesis and secretion. Traffic *10*, 42-56.

des Georges, A., Katsuki, M., Drummond, D.R., Osei, M., Cross, R.A., and Amos, L.A. (2008). Mal3, the Schizosaccharomyces pombe homolog of EB1, changes the microtubule lattice. Nat Struct Mol Biol *15*, 1102-1108.

Diaz, J.F., Valpuesta, J.M., Chacon, P., Diakun, G., and Andreu, J.M. (1998). Changes in microtubule protofilament number induced by Taxol binding to an easily accessible site. Internal microtubule dynamics. J Biol Chem *273*, 33803-33810.

Dumontet, C., and Jordan, M.A. (2010). Microtubule-binding agents: a dynamic field of cancer therapeutics. Nat Rev Drug Discov *9*, 790-803.

Eckert, T., Le, D.T., Link, S., Friedmann, L., and Woehlke, G. (2012). Spastin's microtubule-binding properties and comparison to katanin. PloS one *7*, e50161.

Errico, A., Ballabio, A., and Rugarli, E.I. (2002). Spastin, the protein mutated in autosomal dominant hereditary spastic paraplegia, is involved in microtubule dynamics. Hum Mol Genet *11*, 153-163.

Errico, A., Claudiani, P., D'Addio, M., and Rugarli, E.I. (2004). Spastin interacts with the centrosomal protein NA14, and is enriched in the spindle pole, the midbody and the distal axon. Hum Mol Genet *13*, 2121-2132.

Evans, K., Keller, C., Pavur, K., Glasgow, K., Conn, B., and Lauring, B. (2006). Interaction of two hereditary spastic paraplegia gene products, spastin and atlastin, suggests a common pathway for axonal maintenance. Proc Natl Acad Sci U S A *103*, 10666-10671.

Evans, K.J., Gomes, E.R., Reisenweber, S.M., Gundersen, G.G., and Lauring, B.P. (2005). Linking axonal degeneration to microtubule remodeling by Spastin-mediated microtubule severing. J Cell Biol *168*, 599-606.

Fawcett, D.W., and Porter, K.R. (1954). A Study of the Fine Structure of Ciliated Epithelia. J Morphol *94*, 221-282.

Gigant, B., Curmi, P.A., Martin-Barbey, C., Charbaut, E., Lachkar, S., Lebeau, L., Siavoshian, S., Sobel, A., and Knossow, M. (2000). The 4 A X-ray structure of a tubulin:stathmin-like domain complex. Cell *102*, 809-816.

Harris, P. (1962). Some structural and functional aspects of the mitotic apparatus in sea urchin embryos. J Cell Biol *14*, 475-487.

Hazan, J., Fonknechten, N., Mavel, D., Paternotte, C., Samson, D., Artiguenave, F., Davoine, C.S., Cruaud, C., Durr, A., Wincker, P.*, et al.* (1999). Spastin, a new AAA protein, is altered in the most frequent form of autosomal dominant spastic paraplegia. Nat Genet *23*, 296-303.

Heymann, J.B. (2018). Single particle reconstruction and validation using Bsoft for the map challenge. J Struct Biol *204*, 90-95.

Howard, J. (1997). Molecular motors: structural adaptations to cellular functions. Nature *389*, 561-567.

Kabsch, W., Mannherz, H.G., Suck, D., Pai, E.F., and Holmes, K.C. (1990). Atomic structure of the actin:DNase I complex. Nature *347*, 37-44.

Kellogg, E.H., Hejab, N.M.A., Howes, S., Northcote, P., Miller, J.H., Diaz, J.F., Downing, K.H., and Nogales, E. (2017). Insights into the Distinct Mechanisms of Action of Taxane and Non-Taxane Microtubule Stabilizers from Cryo-EM Structures. J Mol Biol *429*, 633-646.

Kikkawa, M., Ishikawa, T., Nakata, T., Wakabayashi, T., and Hirokawa, N. (1994). Direct visualization of the microtubule lattice seam both in vitro and in vivo. J Cell Biol *127*, 1965-1971.

Kuo, Y.W., Trottier, O., Mahamdeh, M., and Howard, J. (2019). Spastin is a dual-function enzyme that severs microtubules and promotes their regrowth to increase the number and mass of microtubules. Proc Natl Acad Sci U S A *116*, 5533-5541.

Lacey, S.E., He, S., Scheres, S.H., and Carter, A.P. (2019). Cryo-EM of dynein microtubule-binding domains shows how an axonemal dynein distorts the microtubule. Elife *8*.

Larsson, H., Wallin, M., and Edstrom, A. (1976). Induction of a sheet polymer of tubulin by Zn2+. Exp Cell Res *100*, 104-110.

Ledbetter, M.C., and Porter, K.R. (1963). A "Microtubule" in Plant Cell Fine Structure. J Cell Biol *19*, 239-250.

Ledbetter, M.C., and Porter, K.R. (1964). Morphology of Microtubules of Plant Cells. Science *144*, 872-&.

Li, H., DeRosier, D.J., Nicholson, W.V., Nogales, E., and Downing, K.H. (2002). Microtubule structure at 8 A resolution. Structure *10*, 1317-1328.

Liu, D.F., Liu, X.Q., Shang, Z.G., and Sindelar, C.V. (2017). Structural basis of cooperativity in kinesin revealed by 3D reconstruction of a two-head-bound state on microtubules. Elife *6*, 1-21.

Ludtke, S.J., Baldwin, P.R., and Chiu, W. (1999). EMAN: Semiautomated software for high-resolution single-particle reconstructions. J Struct Biol *128*, 82-97.

Manka, S.W., and Moores, C.A. (2018). Microtubule structure by cryo-EM: snapshots of dynamic instability. Essays Biochem *62*, 737-751.

Manton, I., and Clarke, B. (1952). An Electron Microscope Study of the Spermatozoid of Sphagnum. J Exp Bot *3*, 265-&.

McDermott, C.J., Grierson, A.J., Wood, J.D., Bingley, M., Wharton, S.B., Bushby, K.M., and Shaw, P.J. (2003). Hereditary spastic paraparesis: disrupted intracellular transport associated with spastin mutation. Ann Neurol *54*, 748-759.

Mentes, A., Huehn, A., Liu, X., Zwolak, A., Dominguez, R., Shuman, H., Ostap, E.M., and Sindelar, C.V. (2018). High-resolution cryo-EM structures of actin-bound myosin states reveal the mechanism of myosin force sensing. Proc Natl Acad Sci U S A *115*, 1292-1297.

Mitchison, T., and Kirschner, M. (1984). Dynamic instability of microtubule growth. Nature *312*, 237-242.

Molon, A., Di Giovanni, S., Chen, Y.W., Clarkson, P.M., Angelini, C., Pegoraro, E., and Hoffman, E.P. (2004). Large-scale disruption of microtubule pathways in morphologically normal human spastin muscle. Neurology *62*, 1097-1104.

Moores, C.A., Perderiset, M., Francis, F., Chelly, J., Houdusse, A., and Milligan, R.A. (2004). Mechanism of microtubule stabilization by doublecortin. Mol Cell *14*, 833-839.

Nogales, E., Whittaker, M., Milligan, R.A., and Downing, K.H. (1999). High-resolution model of the microtubule. Cell *96*, 79-88.

Nogales, E., Wolf, S.G., and Downing, K.H. (1998). Structure of the alpha beta tubulin dimer by electron crystallography. Nature *391*, 199-203.

Nogales, E., Wolf, S.G., Khan, I.A., Luduena, R.F., and Downing, K.H. (1995). Structure of tubulin at 6.5 A and location of the taxol-binding site. Nature *375*, 424-427.

Pease, D.C. (1963). The Ultrastructure of Flagellar Fibrils. J Cell Biol *18*, 313-326.

Pellegrini, L., Wetzel, A., Granno, S., Heaton, G., and Harvey, K. (2017). Back to the tubule: microtubule dynamics in Parkinson's disease. Cell Mol Life Sci *74*, 409-434.

Pettersen, E.F., Goddard, T.D., Huang, C.C., Couch, G.S., Greenblatt, D.M., Meng, E.C., and Ferrin, T.E. (2004). UCSF chimera - A visualization system for exploratory research and analysis. J Comput Chem *25*, 1605-1612.

Pierson, G.B., Burton, P.R., and Himes, R.H. (1978). Alterations in number of protofilaments in microtubules assembled in vitro. J Cell Biol *76*, 223-228.

Prosser, S.L., and Pelletier, L. (2017). Mitotic spindle assembly in animal cells: a fine balancing act. Nat Rev Mol Cell Biol *18*, 187-201.

Reid, E., Connell, J., Edwards, T.L., Duley, S., Brown, S.E., and Sanderson, C.M. (2005). The hereditary spastic paraplegia protein spastin interacts with the ESCRT-III complex-associated endosomal protein CHMP1B. Hum Mol Genet *14*, 19-38.

Roll-Mecak, A., and Vale, R.D. (2005). The Drosophila homologue of the hereditary spastic paraplegia protein, spastin, severs and disassembles microtubules. Curr Biol *15*, 650-655.

Roll-Mecak, A., and Vale, R.D. (2008). Structural basis of microtubule severing by the hereditary spastic paraplegia protein spastin. Nature *451*, 363-367.

Sandate, C.R., Szyk, A., Zehr, E.A., Lander, G.C., and Roll-Mecak, A. (2019). An allosteric network in spastin couples multiple activities required for microtubule severing. Nat Struct Mol Biol *26*, 671-678.

Scheres, S.H.W. (2012). RELION: Implementation of a Bayesian approach to cryo-EM structure determination. J Struct Biol *180*, 519-530.

Schiff, P.B., Fant, J., and Horwitz, S.B. (1979). Promotion of microtubule assembly in vitro by taxol. Nature *277*, 665-667.

Schiff, P.B., and Horwitz, S.B. (1981). Taxol Assembles Tubulin in the Absence of Exogenous Guanosine 5'-Triphosphate or Microtubule-Associated Proteins. Biochemistry-Us *20*, 3247-3252.

Shang, Z.G., Zhou, K.F., Xu, C., Csencsits, R., Cochran, J.C., and Sindelar, C.V. (2014). High-resolution structures of kinesin on microtubules provide a basis for nucleotide-gated force generation. Elife *3*.

Shelanski, M.L., and Taylor, E.W. (1967). Isolation of a protein subunit from microtubules. J Cell Biol *34*, 549-554.

Sherwood, N.T., Sun, Q., Xue, M., Zhang, B., and Zinn, K. (2004). Drosophila spastin regulates synaptic microtubule networks and is required for normal motor function. PLoS Biol *2*, e429.

Sindelar, C.V., and Downing, K.H. (2007). The beginning of kinesin's force-generating cycle visualized at 9-A resolution. J Cell Biol *177*, 377-385.

Sindelar, C.V., and Downing, K.H. (2010). An atomic-level mechanism for activation of the kinesin molecular motors. P Natl Acad Sci USA *107*, 4111-4116.

Sui, H., and Downing, K.H. (2010). Structural basis of interprotofilament interaction and lateral deformation of microtubules. Structure *18*, 1022-1031.

Svenson, I.K., Kloos, M.T., Jacon, A., Gallione, C., Horton, A.C., Pericak-Vance, M.A., Ehlers, M.D., and Marchuk, D.A. (2005). Subcellular localization of spastin: implications for the pathogenesis of hereditary spastic paraplegia. Neurogenetics *6*, 135-141.

Ti, S.C., Alushin, G.M., and Kapoor, T.M. (2018). Human beta-Tubulin Isotypes Can Regulate Microtubule Protofilament Number and Stability. Dev Cell *47*, 175-190 e175.

Tilney, L.G., Bryan, J., Bush, D.J., Fujiwara, K., Mooseker, M.S., Murphy, D.B., and Snyder, D.H. (1973). Microtubules: evidence for 13 protofilaments. J Cell Biol *59*, 267-275.

Trotta, N., Orso, G., Rossetto, M.G., Daga, A., and Broadie, K. (2004). The hereditary spastic paraplegia gene, spastin, regulates microtubule stability to modulate synaptic structure and function. Curr Biol *14*, 1135-1147.

Valenstein, M.L., and Roll-Mecak, A. (2016). Graded Control of Microtubule Severing by Tubulin Glutamylation. Cell *164*, 911-921.

White, S.R., Evans, K.J., Lary, J., Cole, J.L., and Lauring, B. (2007). Recognition of C-terminal amino acids in tubulin by pore loops in Spastin is important for microtubule severing. J Cell Biol *176*, 995-1005.

Yu, R.C., Hanson, P.I., Jahn, R., and Brunger, A.T. (1998). Structure of the ATP-dependent oligomerization domain of N-ethylmaleimide sensitive factor complexed with ATP. Nat Struct Biol *5*, 803-811.

Zehr, E., Szyk, A., Piszczek, G., Szczesna, E., Zuo, X., and Roll-Mecak, A. (2017). Katanin spiral and ring structures shed light on power stroke for microtubule severing. Nat Struct Mol Biol *24*, 717-725.

Zhang, K. (2016). Gctf: Real-time CTF determination and correction. J Struct Biol *193*, 1-12.

Zhang, R., Alushin, G.M., Brown, A., and Nogales, E. (2015). Mechanistic Origin of Microtubule Dynamic Instability and Its Modulation by EB Proteins. Cell *162*, 849-859.

Zhang, R., LaFrance, B., and Nogales, E. (2018). Separating the effects of nucleotide and EB binding on microtubule structure. P Natl Acad Sci USA *115*, E6191-E6200.

Zhang, R., and Nogales, E. (2015). A new protocol to accurately determine microtubule lattice seam location. J Struct Biol *192*, 245-254.

Zheng, S.Q., Palovcak, E., Armache, J.P., Verba, K.A., Cheng, Y.F., and Agard, D.A. (2017). MotionCor2: anisotropic correction of beam-induced motion for improved cryo-electron microscopy. Nat Methods *14*, 331-332.